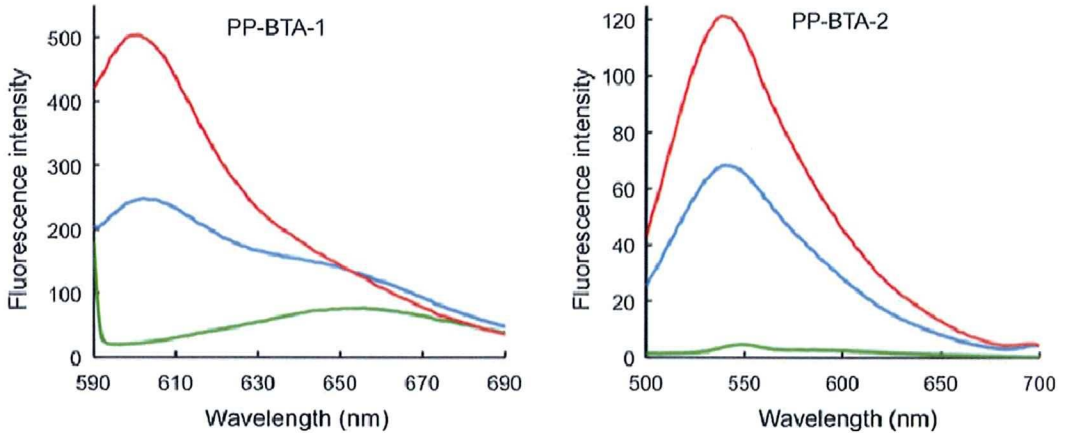

Figure 3. Aβ-dependent change in the fluorescence spectra of PP-BTA-1 and PP-BTA-2. Green, blue and red lines show the fluorescence spectrum of 0, 5 and 10 μg/mL of Aβ(1-42) aggregates, respectively.

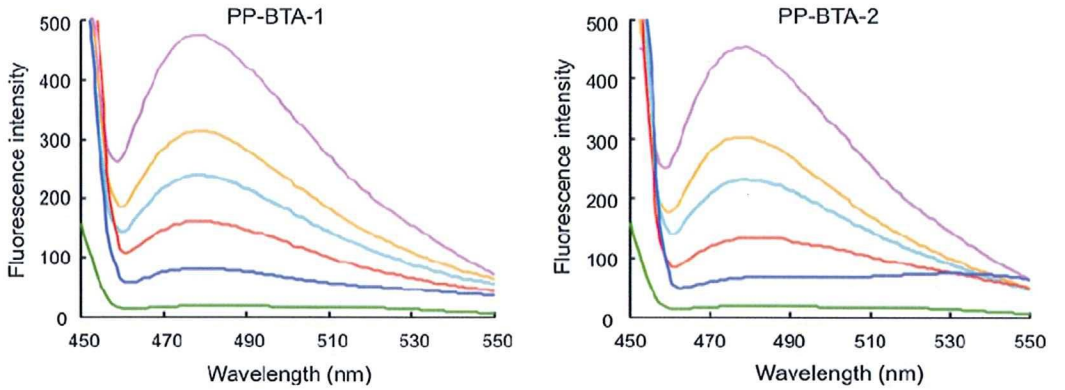

Figure 4. Inhibition assays of PP-BTA-1 and PP-BTA-2 using thioflavin T as the ligand in Aβ(1-42) aggregates. Fluorescence spectral change of thioflavin T (3 μM) upon addition of 0.0611 (orange line), 0.122 (cyan line), 0.486 (red line), or 2.65 (blue line) μM of PP-BTA-1 and PP-BTA-2 to Aβ(1-42) aggregates (10 μg/mL). A pink line shows the fluorescence spectrum of thioflavin T (3 μM) with Aβ(1-42) aggregates. A green line shows the fluorescence spectrum of thioflavin T (3 μM) alone.

Table 1
Apparent inhibition constants (IC_{50}, μM) of benzothiazoles for the binding of thioflavin T to Aβ(1-42) aggregates

Compound	IC_{50}[a] (μM)
PP-BTA-1 (**4**)	0.12 ± 0.001
PP-BTA-2 (**7**)	0.11 ± 0.001
PIB	0.67 ± 0.11

[a] Each value represents the mean ± standard error of the mean for three independent experiments.

PP-BTA-1 and PP-BTA-2 was lower than that of PIB, which is commonly used for clinical research, indicating PP-BTA-1 and PP-BTA-2 to have greater affinity for Aβ(1-42) aggregates. While PP-BTA-1 does not have the phenyl group in the phenylbenzothiazole structure that PIB possesses, it showed stronger binding to Aβ aggregates than PIB. Moreover, benzothiazole is a compact molecule advantageous for penetration of the blood–brain barrier after administration in vivo. These results suggest benzothiazole to be a useful scaffold for the development of Aβ imaging agents in vivo.

Next, the usefulness of PP-BTA-1 and PP-BTA-2 for neuropathological staining of Aβ plaques was investigated in an animal model of AD, the Tg2576 mouse, specifically engineered to overproduce Aβ plaques in the brain. PP-BTA-1 and PP-BTA-2 clearly stained the plaques as reflected by the high affinity for Aβ aggregates in in vitro competition assays (Fig. 5). The labeling pattern was consistent with that observed with thioflavin S. In contrast, wild-type mice displayed no remarkable accumulation of PP-BTA-1 and PP-BTA-2 in brain sections. These results suggest that PP-BTA-1 and PP-BTA-2 show affinity for Aβ plaques in the mouse brain in addition to having affinity for synthetic Aβ(1-42) aggregates.

Furthermore, we also investigated the effectiveness of PP-BTA-1 and PP-BTA-2 for neuropathological staining of Aβ plaques in human AD brain sections (Fig. 6). A previous report suggested the configuration/folding of Aβ plaques in Tg2576 mice to be different from the tertiary/quaternary structure of Aβ plaques in AD brains.[21] Therefore, it is important to evaluate the binding affinity for Aβ plaques in human AD brains. PP-BTA-1 and PP-BTA-2 clearly stained many neuritic plaques in AD brains (Fig. 6A and D). In contrast, no apparent staining was observed in adult normal brain sections (Fig. 6C and F). The labeling pattern was consistent with that observed by immunohistochemical labeling with an antibody specific to Aβ Fig. 6B and E), indicating that PP-BTA-1 and PP-BTA-2 may be applicable for in vivo imaging of Aβ plaques in Alzheimer's brains and deserve further investigation as a potential tool for early diagnosis.

Since PP-BTA-1 and PP-BTA-2 possess a dimethylamino group, they can be used as probes for PET by labeling one of two methyl groups with $^{11}CH_3$. In addition, for the application of push–pull benzothiazole derivatives to optical imaging in vivo, the fine-tuning of absorption/emission wavelengths to a desired region continues by optimizing the combination of donor and acceptor groups.

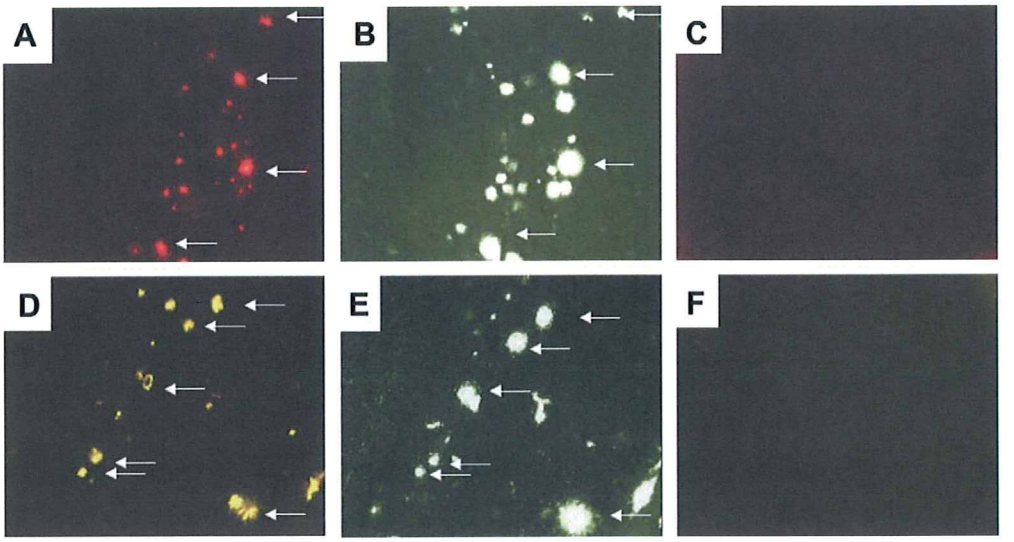

Figure 5. Neuropathological staining of PP-BTA-1 and PP-BTA-2 in 10 μm sections from a mouse model of AD (A and D) and a wild-type mouse (C and F). Aβ plaques labeled with PP-BTA-1 and PP-BTA-2 were confirmed by staining of the serial sections using thioflavin S (B and E).

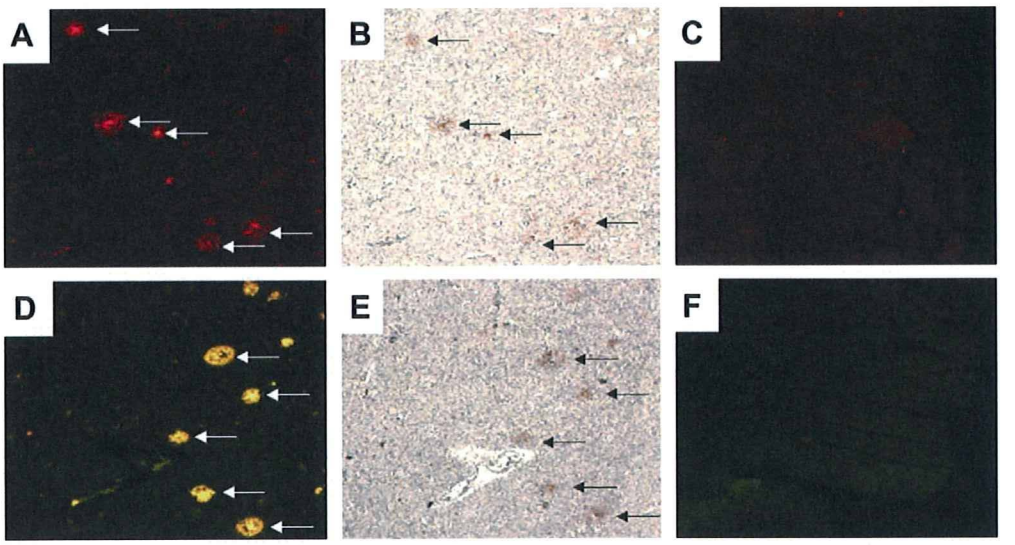

Figure 6. Neuropathological staining of 5 μm AD brain sections from the temporal cortex (A, B, D and E) and adult normal temporal brain sections (C and F). Many neuritic plaques are clearly stained with PP-BTA-1 (A) and PP-BTA-2 (D). Intense fluorescence can be seen in the core of neuritic plaques. Aβ immunostaining with anti Aβ antibodies in the serial sections shows an identical staining pattern of plaques (B and E). No apparent staining was observed in adult normal brain sections (C and F).

3. Conclusion

In conclusion, we successfully designed and synthesized benzothiazole-derived push–pull dyes for imaging Aβ plaques in the brain. In binding experiments in vitro, these benzothiazole compounds showed high affinity for Aβ(1-42) aggregates. PP-BTA-1 and PP-BTA-2 clearly stained Aβ plaques in both mouse brain and human brain, reflecting their affinity for Aβ aggregates in vitro. These findings suggest that additional structural changes on the benzothiazole backbone may be applied to potential Aβ probes for not only optical imaging but also PET and SPECT.

4. Experimental

^{1}H NMR spectra were obtained on a JEOL JNM-LM400 with TMS as an internal standard. Coupling constants are reported in hertz. Multiplicity was defined by s (singlet), d (doublet), t (triplet), br (broad) and m (multiplet). Mass spectra were obtained on a SHIMADZU LCMS-2010 EV. PIB was purchased from ABX (Radeberg, Germany). Other reagents were of reagent grade and used without further purification unless otherwise indicated.

4.1. Chemistry

4.1.1. 1,3-Benzothiazol-6-amine (1)

To a mixture of 6-nitrobenzothiazole (2.5 g, 13.9 mmol) and concentrated HCl (1.93 mL, 22.7 mmol) in 80% EtOH (63 mL) was added powdered iron (3.7 g, 55.6 mmol). The reaction mixture was stirred for 1 h under reflux, and then cooled to room temperature. The precipitate of iron oxides and hydroxy salts was removed by filtration. The solvent was removed and the solid residue was extracted into a heterogeneous mixture of EtOAc (50 mL × 2) and a 10% aqueous solution of Na_2CO_3 (50 mL). The EtOAc extract was dried (Na_2SO_4) and the solvent was removed under vacuum to yield **1** (1.91 g, 91.7%). ^{1}H NMR (400 MHz, $CDCl_3$) δ 8.70 (s, 1H), 7.89 (d, J = 8.8 Hz, 1H), 7.17 (d, J = 2.4 Hz, 1H), 6.87 (dd, J = 8.8, 2.4 Hz, 1H), 3.85 (br s, 2H). MS m/z 151 [MH^+].

4.1.2. *N,N*-Dimethyl-1,3-benzothiazol-6-amine (2)

A solution of **1** (1.47 g, 9.8 mmol) in THF (40 mL) was slowly added to a stirred mixture of 40% aqueous formaldehyde (7.24 mL, 98 mmol) and 4 M H_2SO_4 (7.95 mL, 29.4 mL). Powdered iron (4.36 g, 78.4 mL) was then added and the mixture was vigorously stirred for 3 h. The precipitate of iron salts was removed by filtration and washed with EtOAc (20 mL × 2). The combined organic solutions were made strongly basic with 1 N NaOH (50 mL) and extracted with EtOAc (50 mL × 2). The combined EtOAc extracts were dried (Na_2SO_4) and the solvent was removed on a rotary vacuum evaporator. The oily residue was purified by silica gel chromatography (hexane/EtOAc = 4:1) to give **2** (460 mg, 26.3%). ^{1}H NMR (400 MHz, $CDCl_3$) δ 8.67 (s, 1H), 7.95 (d, J = 8.8 Hz, 1H), 7.15 (d, J = 2.4 Hz, 1H), 7.00 (dd, J = 8.8, 2.4 Hz, 1H), 3.04 (s, 6H). MS m/z 179 [MH^+].

4.1.3. 6-(Dimethylamino)-1,3-benzothiazole-2-carbaldehyde (3)

To a vigorously stirred solution of *n*-BuLi (0.5 mL, 2.6 M in hexane, 1.3 mmol) in THF (5.8 mL) at −78 °C under N_2 was added slowly a solution of **2** (220 mg, 1.23 mmol). The reaction mixture was stirred, warmed to −50 °C and after 1 h cooled to −78 °C. To the resulting solution of aryllithium salt was added slowly anhydrous DMF (0.38 mL). The solution was stirred for 2 h, poured into H_2O (9 mL), neutralized with an aqueous saturated solution of NH_4Cl and subsequently extracted with EtOAc (20 mL × 2). The combined extracts were dried over Na_2SO_4 and the solvent was removed under vacuum to give **3** (255 mg, 97.3%). ^{1}H NMR (400 MHz, $CDCl_3$) δ 10.06 (s, 1H), 8.03 (d, J = 10.0 Hz, 1H), 7.07–7.04 (m, 2H), 3.12 (s, 6H). MS m/z 207 [MH^+].

4.1.4. ((6-(Dimethylamino)-1,3-benzothiazol-2-yl)methylene)-malononitrile (PP-BTA-1, 4)

A solution of **3** (124 mg, 0.6 mmol), malononitrile (60 mg, 0.9 mmol) and pyridine (0.12 mL) in 2-propanol (7.2 mL) was stirred and refluxed for 30 min. The mixture was poured into H_2O (20 mL) and extracted with $CHCl_3$ (20 mL × 3). The combined extracts were dried over Na_2SO_4 and the solvent was removed under vacuum to give **4** (152 mg, 91.7%). ^{1}H NMR (400 MHz, $CDCl_3$) δ 7.99 (s, 1H), 7.99 (d, J = 9.2 Hz, 1H), 7.08 (dd, J = 9.2, 2.4 Hz, 1H), 7.02 (d, J = 2.4 Hz, 1H), 3.16 (s, 6H). MS m/z 255 [MH^+]. Anal. Calcd for $C_{13}H_{10}N_4S$: C, 61.40; H, 3.96; N, 22.03; S, 12.61. Found: C, 61.34; H, 3.84; N, 21.82; S, 12.64.

4.1.5. 4-((*E*)-2-(6-(Dimethylamino)-1,3-benzothiazol-2-yl) vinyl)benzonitrile (5)

To a solution of (4-cyanobenzyl)phosphonate (403.6 mg, 1.6 mmol) in MeOH (12.8 mL) was added NaOMe (0.632 mL). The mixture was cooled in an ice bath, and stirred under reflux for 3 h after the addition of **3** (330 mg, 1.6 mmol). The solid that formed in the reaction mixture was filtered to give **5** (385 mg, 78.8%). ^{1}H NMR (400 MHz, $CDCl_3$) δ 7.84 (d, J = 9.6 Hz, 1H), 7.64 (dd, J = 21.2, 8.0 Hz, 4H), 7.45 (d, J = 16.4 Hz, 1H), 7.32 (d, J = 16.4 Hz, 1H), 7.06 (d, J = 2.8 Hz, 1H), 6.95 (dd, J = 9.6, 2.8 Hz, 1H), 3.06 (s, 6H). MS m/z 306 [MH^+].

4.1.6. 4-((*E*)-2-(6-(Dimethylamino)-1,3-benzothiazol-2-yl) vinyl)benzaldehyde (6)

To a solution of **5** (61 mg, 0.2 mmol) in THF (3.3 mL) was added DIBAL-H (1 M in hexane, 0.5 mL) at −78 °C. The reaction mixture was stirred at room temperature overnight. Thereafter, 10% acetic acid (15 mL) was added and the mixture was extracted with $CHCl_3$ (20 mL × 2). After the organic layer was washed with saline, the combined extracts were dried over Na_2SO_4. The residue was purified by silica gel chromatography (hexane/EtOAc = 2:1) to give **6** (28 mg, 45.4%). ^{1}H NMR (400 MHz, $CDCl_3$) δ 10.02 (s, 1H), 7.90 (d, J = 8.4 Hz, 2H), 7.85 (d, J = 8.2 Hz, 1H), 7.67 (d, J = 8.4 Hz, 2H), 7.50 (d, J = 16.4 Hz, 1H), 7.38 (d, J = 16.4 Hz, 1H), 7.07 (d, J = 2.4 Hz, 1H), 6.96 (dd, J = 8.8, 2.4 Hz, 1H), 3.06 (s, 6H). MS m/z 309 [MH^+].

4.1.7. 4-((*E*)-2-(6-(Dimethylamino)-1,3-benzothiazol-2-yl) vinyl)benzylidene)malononitrile (PP-BTA-2, 7)

The same reaction as described above to prepare **5** was used, and 45 mg of **7** was obtained in a 63.5% yield from **6**. ^{1}H NMR (400 MHz, $CDCl_3$) δ 7.94 (d, J = 8.4 Hz, 2H), 7.86 (d, J = 8.8 Hz, 1H), 7.73 (s, 1H), 7.68 (d, J = 8.4 Hz, 2H), 7.53 (d, J = 16.4 Hz, 1H), 7.35 (d, J = 16.4 Hz, 1H), 7.08 (s, 1H), 6.97 (d, J = 10.0 Hz , 1H), 3.08 (s, 6H). MS m/z 357 [MH^+]. Anal. Calcd for $C_{21}H_{16}N_4S$: C, 70.76; H, 4.52; N, 15.72; S, 9.00. Found: C, 70.48; H, 4.57; N, 15.43; S, 8.99.

4.2. Fluorescence experiments

PP-BTA-1 and PP-BTA-2 were dissolved in 5% EtOH at 10 μM. The fluorescence of PP-BTA-1 and PP-BTA-2 was measured with a spectrophotometer (RF-1500, Shimadzu, Japan). For some measurements, the spectra of PP-BTA-1 and PP-BTA-2 were determined with or without Aβ(1-42) aggregates (0, 5 and 10 μM).

4.3. Binding experiments using Aβ(1-42) aggregates

A solid form of Aβ(1-42) was purchased from Peptide Institute (Osaka, Japan). Aggregation was carried out by gently dissolving the peptide (0.25 mg/mL) in a buffer solution (pH 7.4) containing 10 mM sodium phosphate and 1 mM EDTA. The solution was incubated at 37 °C for 42 h with gentle and constant shaking. Thioflavin-T was used as the tracer for the competition binding experiments. A mixture (3.6 mL of 10% EtOH) containing PP-BTA-1, PP-BTA-2 and PIB (final concn 61.1 nM–5.48 μM), thioflavin-T (final concn 3 μM), and Aβ(1-42) aggregates (final concn 10 μg/mL) was incubated at room temperature for 10 min. Fluorescence intensity at an excitation wavelength of 445 nm was plotted, and values for the apparent half-maximal inhibitory concentration (IC_{50}) were determined from a calibration curve of fluorescence intensity at 478 nm in three independent experiments.

4.4. Staining of Aβ plaques in Tg2576 mouse brain sections

The experiments with animals were conducted in accordance with our institutional guidelines and approved by the Kyoto University Animal Care Committee. The Tg2576 transgenic mice (female, 27-month-old) and wild-type mice (female, 27-month-old) were used as the Alzheimer's model and control mice, respectively. After the mice were sacrificed by decapitation, the brains were immediately removed and frozen in powdered dry ice. The frozen blocks were sliced into serial sections, 10 μm thick. Each slide was incubated with a 50% EtOH solution (100 μM) of PP-BTA-1 and PP-BTA-2 for 10 min. The sections were washed in 50% EtOH for 1 min two times, and examined using a microscope (Nikon Eclipse 80i) equipped with a G-2A filter set (excitation, 510–560 nm; diachronic mirror, 575 nm; longpass filter, 470 nm) for PP-BTA-1, and a B-2A filter set (excitation, 450–480 nm; diachronic mirror, 505 nm; longpass filter, 520 nm) for PP-BTA-2. Thereafter, the serial sections were also stained with thioflavin S, a pathological dye commonly used for staining Aβ plaques in the brain, and examined using a microscope (Nikon Eclipse 80i) equipped with a BV-2A filter set (excitation, 400–440 nm; diachronic mirror, 455 nm; longpass filter, 470 nm).

4.5. Staining of Aβ plaques in human AD brain sections

Postmortem brain tissues from an autopsy-confirmed case of AD (73-year-old male) and a control subject (36-year-old male) were

obtained from BioChain Institute Inc. The sections were incubated with PP-BTA-1 and PP-BTA-2 (50% EtOH, 100 μM) for 10 min at room temperature. The sections were washed in 50% EtOH for 1 min two times, and examined using a microscope (Nikon Eclipse 80i) equipped with a G-2A filter set (excitation, 510–560 nm; diachronic mirror, 575 nm; longpass filter, 470 nm) for PP-BTA-1, and a B-2A filter set (excitation, 450–480 nm; diachronic mirror, 505 nm; longpass filter, 520 nm) for PP-BTA-2. The presence and localization of plaques on the same sections were confirmed with immunohistochemical staining using a monoclonal Aβ antibody, BC05 (Wako).

Acknowledgements

This study was supported by the Program for Promotion of Fundamental Studies in Health Sciences of the National Institute of Biomedical Innovation (NIBIO), a Health Labour Sciences Research Grant, and a Grant-in-Aid for Young Scientists (A) and Exploratory Research from the Ministry of Education, Culture, Sports, Science and Technology, Japan.

References and notes

1. Klunk, W. E. *Neurobiol. Aging* **1998**, *19*, 145.
2. Selkoe, D. J. *Physiol. Rev.* **2001**, *81*, 741.
3. Shoghi-Jadid, K.; Small, G. W.; Agdeppa, E. D.; Kepe, V.; Ercoli, L. M.; Siddarth, P.; Read, S.; Satyamurthy, N.; Petric, A.; Huang, S. C.; Barrio, J. R. *Am. J. Geriatr. Psychiat.* **2002**, *10*, 24.
4. Mathis, C. A.; Wang, Y.; Holt, D. P.; Huang, G. F.; Debnath, M. L.; Klunk, W. E. *J. Med. Chem.* **2003**, *46*, 2740.
5. Ono, M.; Wilson, A.; Nobrega, J.; Westaway, D.; Verhoeff, P.; Zhuang, Z. P.; Kung, M. P.; Kung, H. F. *Nucl. Med. Biol.* **2003**, *30*, 565.
6. Klunk, W. E.; Engler, H.; Nordberg, A.; Wang, Y.; Blomqvist, G.; Holt, D. P.; Bergstrom, M.; Savitcheva, I.; Huang, G. F.; Estrada, S.; Ausen, B.; Debnath, M. L.; Barletta, J.; Price, J. C.; Sandell, J.; Lopresti, B. J.; Wall, A.; Koivisto, P.; Antoni, G.; Mathis, C. A.; Langstrom, B. *Ann. Neurol.* **2004**, *55*, 306.
7. Verhoeff, N. P.; Wilson, A. A.; Takeshita, S.; Trop, L.; Hussey, D.; Singh, K.; Kung, H. F.; Kung, M. P.; Houle, S. *Am. J. Geriatr. Psychiat.* **2004**, *12*, 584.
8. Small, G. W.; Kepe, V.; Ercoli, L. M.; Siddarth, P.; Bookheimer, S. Y.; Miller, K. J.; Lavretsky, H.; Burggren, A. C.; Cole, G. M.; Vinters, H. V.; Thompson, P. M.; Huang, S. C.; Satyamurthy, N.; Phelps, M. E.; Barrio, J. R. *N. Eng. J. Med.* **2006**, *355*, 2652.
9. Kudo, Y.; Okamura, N.; Furumoto, S.; Tashiro, M.; Furukawa, K.; Maruyama, M.; Itoh, M.; Iwata, R.; Yanai, K.; Arai, H. *J. Nucl. Med.* **2007**, *48*, 553.
10. Rowe, C. C.; Ackerman, U.; Browne, W.; Mulligan, R.; Pike, K. L.; O'Keefe, G.; Tochon-Danguy, H.; Chan, G.; Berlangieri, S. U.; Jones, G.; Dickinson-Rowe, K. L.; Kung, H. P.; Zhang, W.; Kung, M. P.; Skovronsky, D.; Dyrks, T.; Holl, G.; Krause, S.; Friebe, M.; Lehman, L.; Lindemann, S.; Dinkelborg, L. M.; Masters, C. L.; Villemagne, V. L. *Lancet. Neurol.* **2008**, *7*, 129.
11. Higuchi, M.; Iwata, N.; Matsuba, Y.; Sato, K.; Sasamoto, K.; Saido, T. C. *Nat. Neurosci.* **2005**, *8*, 527.
12. Poduslo, J. F.; Curran, G. L.; Peterson, J. A.; McCormick, D. J.; Fauq, A. H.; Khan, M. A.; Wengenack, T. M. *Biochemistry* **2004**, *43*, 6064.
13. Bacskai, B. J.; Frosch, M. P.; Freeman, S. H.; Raymond, S. B.; Augustinack, J. C.; Johnson, K. A.; Irizarry, M. C.; Klunk, W. E.; Mathis, C. A.; Dekosky, S. T.; Greenberg, S. M.; Hyman, B. T.; Growdon, J. H. *Arch. Neurol.* **2007**, *64*, 431.
14. Johnson, K. A.; Gregas, M.; Becker, J. A.; Kinnecom, C.; Salat, D. H.; Moran, E. K.; Smith, E. E.; Rosand, J.; Rentz, D. M.; Klunk, W. E.; Mathis, C. A.; Price, J. C.; Dekosky, S. T.; Fischman, A. J.; Greenberg, S. M. *Ann. Neurol.* **2007**, *62*, 229.
15. Pike, K. E.; Savage, G.; Villemagne, V. L.; Ng, S.; Moss, S. A.; Maruff, P.; Mathis, C. A.; Klunk, W. E.; Masters, C. L.; Rowe, C. C. *Brain* **2007**, *130*, 2837.
16. Hintersteiner, M.; Enz, A.; Frey, P.; Jaton, A. L.; Kinzy, W.; Kneuer, R.; Neumann, U.; Rudin, M.; Staufenbiel, M.; Stoeckli, M.; Wiederhold, K. H.; Gremlich, H. U. *Nat. Biotechnol.* **2005**, *23*, 577.
17. Nesterov, E. E.; Skoch, J.; Hyman, B. T.; Klunk, W. E.; Bacskai, B. J.; Swager, T. M. *Angew. Chem., Int. Ed. Engl.* **2005**, *44*, 5452.
18. Raymond, S. B.; Skoch, J.; Hills, I. D.; Nesterov, E. E.; Swager, T. M.; Bacskai, B. J. *Eur. J. Nucl. Med. Mol. Imaging* **2008**, *35*, S93.
19. Hrobarik, P.; Sigmundova, I.; Zahradnik, P. *Synthesis* **2005**, *4*, 600.
20. Cho, B. R.; Chajara, K.; Jung, H.; Son, K. H.; Jeon, S. J. *Org. Lett.* **2002**, *4*, 1703.
21. Toyama, H.; Ye, D.; Ichise, M.; Liow, J. S.; Cai, L.; Jacobowitz, D.; Musachio, J. L.; Hong, J.; Crescenzo, M.; Tipre, D.; Lu, J. Q.; Zoghbi, S.; Vines, D. C.; Seidel, J.; Katada, K.; Green, M. V.; Pike, V. W.; Cohen, R. M.; Innis, R. B. *Eur. J. Nucl. Med. Mol. Imaging* **2005**, *32*, 593.

Novel Radioiodinated Aurones as Probes for SPECT Imaging of β-Amyloid Plaques in the Brain

Yoshifumi Maya,[†] Masahiro Ono,*[,†,‡] Hiroyuki Watanabe,[†] Mamoru Haratake,[†] Hideo Saji,[‡] and Morio Nakayama*[,†]

Department of Hygienic Chemistry, Graduate School of Biomedical Sciences, Nagasaki University, 1-14 Bunkyo-machi, Nagasaki 852-8521, and Department of Patho-Functional Bioanalysis, Graduate School of Pharmaceutical Sciences, Kyoto University, 46−29 Yoshida Shimoadachi-cho, Sakyo-ku, Kyoto 606-8501, Japan. Received July 29, 2008; Revised Manuscript Received November 10, 2008

We report a novel series of radioiodinated aurone derivatives as probes for imaging Aβ plaques in the brains of patients with Alzheimer's disease (AD) using single photon emission computed tomography (SPECT). In binding experiments in vitro, aurone derivatives showed very good affinity for Aβ aggregates (K_i = 1.1 to 3.4 nM). No-carrier-added radioiodinated aurones were successfully prepared through an iododestannylation reaction from the corresponding tributyltin derivatives. In biodistribution experiments using normal mice, aurone derivatives displayed high brain uptake (1.7−4.5% ID/g at 2 min) and rapid clearance from the brain (0.1−0.4% ID/g at 30 min), especially [^{125}I]**15**. Furthermore, a specific plaque labeling signal was observed in in vitro autoradiography of postmortem AD brain sections using [^{125}I]**15**. [^{125}I]**15** may be a useful SPECT imaging agent for detecting Aβ plaques in the brain of AD.

INTRODUCTION

Alzheimer's disease (AD) is a progressive neurodegenerative disorder characterized by cognitive decline, irreversible memory loss, disorientation, and language impairment. Senile plaques containing β-amyloid (Aβ) peptides and neurofibrillary tangles in the postmortem brain are two pathological hallmarks of AD (*1, 2*). Excessive production of Aβ via various normal or abnormal mechanisms is considered to be the initial neurodegenerative event in AD. Currently, it is difficult for clinicians to differentiate between the cognitive decline associated with normal aging and the cognitive decline associated with AD. There is no simple and definitive diagnostic method to detect Aβ plaques in the brain without postmortem pathological staining of brain tissue. Thus, the development of imaging agents for positron emission tomography (PET) or single photon emission computed tomography (SPECT), which can detect Aβ plaques in vivo, may assist with the early diagnosis of AD (*3−5*).

In the past few years, several groups have reported potential amyloid-imaging probes for the detection of Aβ plaques in vivo. Tracers such as [^{11}C]PIB (*6, 7*), [^{11}C]SB-13 (*8, 9*), [^{18}F]BAY94-9172 (*10*), [^{11}C]BF-227 (*11*), [^{18}F]FDDNP (*12−14*), and [^{123}I]IMPY (*15−18*) have been tested clinically and demonstrated utility (Figure 1). [^{123}I]IMPY is the only tracer for SPECT; the other five tracers are amyloid imaging probes for PET. Since SPECT is more valuable than PET in terms of routine diagnostic use, the development of more useful β-amyloid-imaging agents for SPECT has been a critical issue.

Recently, we have reported that radioiodinated aurones possessing a nucleophilic group (NH_2, NHMe, and NMe_2) function as a new backbone structure in the development of amyloid-imaging probes for SPECT (*19*). These compounds showed strong binding to Aβ aggregates (K_i = 1.2−6.8 nM), good penetration of the brain (1.9−4.6% ID/g at 2 min), and a fast washout from the brain (0.3−0.5% ID/g at 30 min). However, the aurone derivatives appeared inferior to IMPY in pharmacokinetics, although their high affinity for β-amyloid plaques is sufficient for imaging in vivo. Therefore, additional structural changes are essential to further improve the properties of aurone derivatives to make them suitable for the imaging of β-amyloid plaques in the brain.

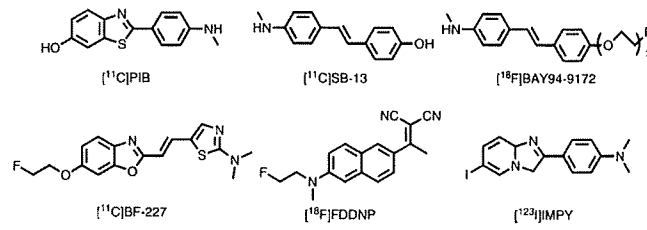

Figure 1. Chemical structure of Aβ imaging probes clinically tested.

To develop more promising aurones for SPECT-based imaging of β-amyloid plaques, we designed a novel series of radioiodinated derivatives with poly(ethylene glycol) (PEG). PEG is nontoxic, nonimmunogenic, highly soluble in water, and FDA-approved, and PEGylation has been used to change the pharmacokinetics of various biologically interesting proteins or peptides, leading to better therapeutics (*20, 21*). Therefore, PEGylated aurone derivatives are worthy of further evaluation as novel β-amyloid-imaging probes for SPECT.

In the present study, we designed and synthesized a novel series of radioiodinated aurone derivatives with not only 1 to 3 units of ethylene glycol at the 4′ position, but also other nucleophilic groups (-OCH_3 and -OH), and evaluated their biological potential as probes for imaging β-amyloid by testing their affinity for Aβ aggregates in vitro and their uptake by and

* To whom correspondence should be addressed. Phone +81-75-753-4608, Fax +81-75-753-4568, e-mail ono@pharm.kyoto-u.ac.jp for M. Ono. Phone +81-95-819-2441, Fax +81-95-819-2441, e-mail morio@nagasaki-u.ac.jp for M. Nakayama.
† Nagasaki University.
‡ Kyoto University.

10.1021/bc8003292 CCC: $40.75
Published on Web 12/11/2008

clearance from the brain in biodistribution experiments using normal mice.

MATERIALS AND METHODS

All reagents were commercial products and used without further purification unless otherwise indicated. ^{1}H NMR spectra were obtained on a Varian Gemini 300 spectrometer with TMS as an internal standard. Coupling constants are reported in hertz. Multiplicity was defined by s (singlet), d (doublet), t (triplet), and m (multiplet). Mass spectra were obtained on a JEOL IMS-DX instrument.

Chemistry. *Methyl 2-((Ethoxycarbonyl)methoxy)-5-bromobenzoate (**1**).* To a solution of 2-hydroxy-5-bromobenzoic acid methyl ester (1.5 g, 6.49 mmol) in acetone (10 mL) was added K_2CO_3 (2.7 g, 19.5 mmol) and ethylbromoacetate (1.3 mL, 7.78 mmol). The mixture was stirred for 3 h under reflux. After the solvent was evaporated, the residue was dissolved in water (100 mL) and extracted with ethyl acetate (100 mL). The organic layer was dried over Na_2SO_4, and evaporation of the solvent gave 1.60 g of **1** (77.7%). ^{1}H NMR NMR (300 MHz, $CDCl_3$) δ 1.29 (t, J = 7.2 Hz, 3H), 3.91 (s, 3H), 4.24 (q, J = 7.2 Hz, 2H), 4.69 (s, 2H), 6.78 (d, J = 9.0 Hz, 1H), 7.54 (d, J = 6.3 Hz, 1H), 7.96 (s, 1H).

*2-(Carboxymethoxy)-5-bromobenzoic Acid (**2**).* To a solution of **1** (1.6 g, 5.04 mmol) in methanol (10 mL) was added 10% aqueous KOH (3.0 mL). The mixture was stirred for 2 h at room temperature. The product formed by adding 1 N HCl was filtered to give 1.10 g of **2** (79.4%). ^{1}H NMR (300 MHz, CD_3OD) δ 4.81 (s, 2H), 7.02 (d, J = 8.7 Hz, 1H), 7.63 (dd, J = 2.4, 2.7 Hz, 1H), 7.93 (d, J = 2.4 Hz, 1H).

*5-Bromo-3-acetoxybenzofuran (**3**).* A mixture of acetic anhydride (20 mL), acetic acid (4 mL), anhydrous sodium acetate (1.0 g, 12.0 mmol), and **2** (100 mg, 0.36 mmol) was heated to reflux for 5 h. Water (100 mL) was then added, and the mixture was extracted with chloroform (100 mL). After drying of the organic layer on Na_2SO_4, evaporation gave 78 mg of **3** (86.5%). ^{1}H NMR (300 MHz, $CDCl_3$) δ 2.37 (s, 3H), 7.33 (d, J = 9.0 Hz, 1H), 7.43 (dd, J = 3.6, 2.1 Hz, 1H), 7.71 (s, 1H), 8.02 (s, 1H).

*5-Bromobenzofuran-3(2H)-one (**4**).* A mixture of **3** (78 mg, 0.31 mmol), methanol (3 mL), water (1 mL), and 1 N HCl (2 mL) was heated to reflux for 3 h. The precipitate formed was collected by filtration, washed with water, and dried under vacuum to obtain 15 mg of **4** (22.5%). ^{1}H NMR (300 MHz, $CDCl_3$) δ 4.67 (s, 2H), 7.06 (d, J = 9.0 Hz, 1H), 7.69 (dd, J = 2.1, 2.1 Hz, 1H), 7.79 (d, J = 2.1 Hz, 1H).

*(Z)-2-(4-Methoxybenzylidene)-5-bromobenzofuran-3(2H)-one (**5**).* To a solution of **4** (300 mg, 1.41 mmol) and 4-methoxybenzaldehyde (192 mg, 1.41 mmol) in chloroform (5 mL) was added Al_2O_3 (2.7 g, 26.0 mmol). The mixture was stirred for 20 min at room temperature. After filtration of the reaction mixture, the solvent of the filtrate was removed, and drying under vacuum yielded 410 mg of **5** (85.7%). ^{1}H NMR (300 MHz, $CDCl_3$) δ 3.88 (s, 3H), 6.91 (s, 1H), 6.99 (d, J = 9.0 Hz, 2H), 7.24 (d, J = 8.4 Hz, 1H), 7.73 (dd, J = 2.1, 2.1 Hz, 1H), 7.88 (d, J = 8.7 Hz, 2H), 7.92 (d, J = 1.8 Hz, 1H).

*(Z)-2-(4-Hydroxybenzylidene)-5-bromobenzofuran-3(2H)-one (**6**).* BBr_3 (3 mL, 1 M solution in CH_2Cl_2) was added to a solution of **5** (300 mg, 0.91 mmol) in CH_2Cl_2 (25 mL) dropwise in an ice bath. The mixture was allowed to warm to room temperature and stirred for 15 h. Water (50 mL) was added while the reaction mixture was cooled in an ice bath. The mixture was extracted with chloroform (2 × 30 mL), and the organic phase was dried over Na_2SO_4 and filtered. The filtrate was concentrated and the residue was purified by silica gel chromatography (hexane/ethyl acetate = 2:3) to give 15 mg of **6** (5.2%). ^{1}H NMR (300 MHz, DMSO-d_6) δ 1.23 (s, 1H), 6.92 (d, J = 8.4 Hz, 2H), 6.96 (s, 1H), 7.56 (d, J = 9.3 Hz, 1H), 7.88–7.92 (m, 3H), 7.95 (s, 1H). MS (EI) m/z 316 [M^+].

*(Z)-2-(4-Methoxybenzylidene)-5-(tributylstannyl)benzofuran-3(2H)-one (**7**).* A mixture of **5** (200 mg, 0.60 mmol), $(Bu_3Sn)_2$ (0.4 mL), and $(Ph_3P)_4Pd$ (50 mg, 0.043 mmol) in a mixed solvent (15 mL, 1:1 dioxane/Et_3N) was stirred under reflux for 24 h. The solvent was removed, and the resulting residue was purified by silica gel chromatography using chloroform to give 50 mg of **7** (15.3%). ^{1}H NMR (300 MHz, $CDCl_3$) δ 0.89–1.64 (m, 27H), 3.87 (s, 3H), 6.89 (s, 1H), 6.99 (d, J = 8.7 Hz, 2H), 7.31 (d, J = 8.1 Hz, 1H), 7.71 (dd, J = 0.9, 0.9 Hz, 1H), 7.86 (d, J = 9.0 Hz, 2H), 7.90 (d, J = 8.7 Hz 1H). MS (EI) m/z 528 [M^+].

*(Z)-2-(4-Hydroxybenzylidene)-5-(tributylstannyl)benzofuran-3(2H)-one (**8**).* The same reaction as described above to prepare **7** was used, and 10 mg of **8** was obtained in a 12.0% yield from **6**. ^{1}H NMR (300 MHz, $CDCl_3$) δ 0.86–1.60 (m, 27H), 6.74 (d, J = 9.0 Hz, 2H), 6.90 (s, 1H), 7.30 (d, J = 8.1 Hz, 1H), 7.69 (d, J = 8.1 Hz, 1H), 7.80 (d, J = 8.4 Hz, 2H), 7.89 (s, 1H). MS (EI) m/z 542 [M^+].

*(Z)-2-(4-Methoxybenzylidene)-5-iodobenzofuran-3(2H)-one (**9**).* To a solution of **7** (10 mg, 0.03 mmol) in $CHCl_3$ (3 mL) was added a solution of iodine in $CHCl_3$ (1 mL, 0.25 M) at room temperature. The mixture was stirred at room temperature for 5 min, and saturated $NaHSO_3$ solution (15 mL) was added. The organic phase was separated, dried over Na_2SO_4, and filtered. The solvent was removed, and the residue was purified by preparative TLC (2:3 hexane/ethyl acetate) to give 6 mg of **9** (84.0%). ^{1}H NMR (300 MHz, $CDCl_3$) δ 3.88 (s, 3H), 6.91 (s, 1H), 6.98 (d, J = 6.9 Hz, 2H), 7.14 (d, J = 8.4 Hz, 1H), 7.87–7.91 (m, 3H), 8.12 (d, J = 2.1 Hz, 1H). HRMS (EI) m/z calcd for $C_{16}H_{11}O_3I$ (M^+) 377.9753, found 377.9753.

*Methyl 2-((Ethoxycarbonyl)methoxy)-5-iodobenzoate (**10**).* The same reaction as described above to prepare **1** was used, and 2.62 g of **10** was obtained in a 99.0% yield from 2-hydroxy-5-iodobenzoic acid methyl ester. ^{1}H NMR (300 MHz, $CDCl_3$) δ 1.29 (t, J = 7.2 Hz, 3H), 3.90 (s, 3H), 4.25 (q, J = 6.0 Hz, 2H), 4.69 (s, 2H), 6.66 (d, J = 8.7 Hz, 1H), 7.71 (dd, J = 2.4, 2.4 Hz, 1H), 8.12 (d, J = 2.1 Hz, 1H).

*2-(Carboxymethoxy)-5-iodobenzoic Acid (**11**).* The same reaction as described above to prepare **2** was used, and 2.02 g of **11** was obtained in a 87.2% yield from **10**. ^{1}H NMR (300 MHz, CD_3OD) δ 4.81 (s, 2H), 6.89 (d, J = 9.0 Hz, 1H), 7.80 (dd, J = 2.7, 2.4 Hz, 1H), 8.10 (d, J = 2.4 Hz, 1H).

*5-Iodo-3-acetoxybenzofuran (**12**).* The same reaction as described above to prepare **3** was used, and 1.45 g of **12** was obtained in a 76.6% yield from **11**. ^{1}H NMR (300 MHz, $CDCl_3$) δ 2.37 (s, 3H), 7.23 (d, J = 8.1 Hz, 1H), 7.59 (dd, J = 1.5, 1.8 Hz, 1H), 7.90 (d, J = 1.5 Hz, 1H), 7.98 (s, 1H).

*5-Iodobenzofuran-3(2H)-one (**13**).* The same reaction as described above to prepare **4** was used, and 1.17 g of **13** was obtained in a 93.8% yield from **12**. ^{1}H NMR (300 MHz, $CDCl_3$) δ 4.65 (s, 2H), 6.96 (d, J = 9.0 Hz, 1H), 7.85 (dd, J = 1.8, 1.8 Hz, 1H), 7.99 (d, J = 1.8 Hz, 1H).

*(Z)-2-(4-Hydroxybenzylidene)-5-iodobenzofuran-3(2H)-one (**14**).* The same reaction as described above to prepare **5** was used, and 78 mg of **14** was obtained in a 87.0% yield from **13** and 4-hydroxybenzaldehyde. ^{1}H NMR (300 MHz, $CDCl_3$) δ 1.28 (s, 1H), 6.87 (s, 1H), 6.91 (d, J = 5.4 Hz, 2H), 7.29 (d, J = 8.7 Hz, 1H), 7.85 (d, J = 6.9 Hz, 2H), 8.12 (d, J = 6.9 Hz, 1H), 8.08 (d, J = 1.8 Hz, 1H). HRMS (EI) m/z calcd for $C_{15}H_9O_3I$ (M^+) 363.9596, found 363.9571.

*(Z)-2-(4-(2-Hydroxyethoxy)benzylidene)-5-iodobenzofuran-3(2H)-one (**15**).* A mixture of potassium carbonate (3.7 g, 26.8 mmol), **14** (194 mg, 0.53 mmol), and ethylene chlorohydrin (0.1 mL, 1.43 mmol) in anhydrous DMF (7 mL) was heated at 120 °C for 15 h. After cooling to room temperature, water was added,

and the reaction mixture was extracted with ethyl acetate. The organic layer was separated, dried over Na_2SO_4, and evaporated. The resulting residue was purified by silica gel chromatography using ethyl acetate to give 123 mg of **15** (56.5%). ^{1}H NMR (300 MHz, $CDCl_3$) δ 2.01 (s, 1H), 4.02 (s, 2H), 4.18 (t, J = 3.9 Hz, 2H), 6.89 (s, 1H), 7.00 (d, J = 7.5 Hz, 2H), 7.14 (d, J = 8.4 Hz, 1H), 7.80−7.92 (m, 3H), 8.12 (d, J = 1.8 Hz, 1H). HRMS (EI) *m/z* calcd for $C_{17}H_{13}O_4I$ (M^+) 407.9859, found 407.9879.

*(Z)-2-(4-(2-(2-Hydroxyethoxy)ethoxy)benzylidene)-5-iodobenzofuran-3(2H)-one (**16**).* The same reaction as described above to prepare **15** was used, and 56 mg of **16** was obtained in a 30.2% yield from **14** and ethylene glycol mono-2-chloroethyl ether. ^{1}H NMR (300 MHz, $CDCl_3$) δ 2.17 (s, 1H), 3.70 (d, J = 4.8 Hz, 2H), 3.78 (d, J = 4.8 Hz, 2H), 3.92 (t, J = 4.8 Hz, 2H), 4.21 (t, J = 4.5 Hz, 2H), 6.89 (s, 1H), 7.00 (d, J = 11.4 Hz, 2H), 7.13 (d, J = 8.7 Hz, 1H), 7.84−7.91 (m, 3H), 8.11 (d, J = 2.1 Hz, 1H). HRMS (EI) *m/z* calcd for $C_{19}H_{17}O_5I$ (M^+) 452.0121, found 452.0131.

*(Z)-2-(4-(2-(2-(2-Hydroxyethoxy)ethoxy)ethoxy)benzylidene)-5-iodobenzofuran-3(2H)-one (**17**).* The same reaction as described above to prepare **15** was used, and 140 mg of **17** was obtained in a 67.9% yield from **14** and 2-[2-(2-chloroethoxy)ethoxy] ethanol. ^{1}H NMR (300 MHz, $CDCl_3$) δ 1.96 (s, 1H), 3.74−3.80 (m, 6H), 3.92 (t, J = 4.8 Hz, 2H), 4.24 (t, J = 4.8 Hz, 2H), 4.45 (t, J = 4.5 Hz, 1H), 4.65 (t, J = 4.5 Hz, 1H), 6.91 (s, 1H), 6.98 (d, J = 9.0 Hz, 2H), 7.15 (d, J = 8.7 Hz, 1H), 7.85−7.92 (m, 3H), 8.15 (d, J = 2.1 Hz, 1H). HRMS (EI) *m/z* calcd for $C_{21}H_{21}O_6I$ (M^+) 496.0383, found 496.0381.

*(Z)-2-(4-(2-Hydroxyethoxy)benzylidene)-5-(tributylstannyl)benzofuran-3(2H)-one (**18**).* The same reaction as described above to prepare **7** was used, and 7 mg of **18** was obtained in a 25.0% yield from **15**. ^{1}H NMR (300 MHz, $CDCl_3$) δ 0.86−1.61 (m, 27H), 2.06 (s, 1H), 4.02 (s, 2H), 4.16 (t, J = 3.6 Hz, 2H), 6.88 (s, 1H), 6.99 (d, J = 9.0 Hz, 2H), 7.30 (d, J = 12.3 Hz, 1H), 7.73 (d, J = 9.0 Hz, 1H), 7.90−7.92 (m, 3H). MS (EI) *m/z* 572 [M^+].

*(Z)-2-(4-(2-(2-Hydroxyethoxy)ethoxy)benzylidene)-5-(tributylstannyl)benzofuran-3(2H)-one (**19**).* The same reaction as described above to prepare **7** was used, and 17 mg of **19** was obtained in a 31.4% yield from **16**. ^{1}H NMR (300 MHz, $CDCl_3$) δ 0.86−1.32 (m, 27H), 2.11 (s, 1H), 3.70 (t, J = 4.8 Hz, 2H), 3.78 (t, J = 4.8 Hz, 2H), 3.91 (t, J = 4.5 Hz, 2H), 4.22 (t, J = 5.1 Hz, 2H), 6.89 (s, 1H), 7.00 (d, J = 7.2 Hz, 2H), 7.31 (d, J = 8.1 Hz, 1H), 7.71 (d, J = 9.0 Hz, 1H), 7.88−7.91 (m, 3H). MS (EI) *m/z* 616 [M^+].

*(Z)-2-(4-(2-(2-(2-Hydroxyethoxy)ethoxy)ethoxy)benzylidene)-5-(tributylstannyl)benzofuran-3(2H)-one (**20**).* The same reaction as described above to prepare **7** was used, and 4 mg of **20** was obtained in a 30.3% yield from **17**. ^{1}H NMR (300 MHz, $CDCl_3$) δ 0.86−1.59 (m, 27H), 2.11 (s, 1H), 3.63 (t, J = 3.3 Hz, 2H), 3.73−3.75 (m, 4H), 3.90 (t, J = 4.2 Hz, 2H), 4.21 (t, J = 4.2 Hz, 2H), 6.88 (s, 1H), 7.10 (d, J = 8.7 Hz, 2H), 7.31 (d, J = 8.1 Hz, 1H), 7.64−7.70 (m, 3H), 7.90 (d, J = 4.8 Hz, 1H). MS (EI) *m/z* 659 [M^+].

Iododestannylation Reaction. The radioiodinated forms of compounds **9**, **14**, **15**, **16**, and **17** were prepared from the corresponding tributyltin derivatives by iododestannylation. Briefly, to initiate the reaction, the tributyltin derivative (50 μg/50 μL EtOH) was added to a mixture of a [^{125}I]NaI (3.7−7.4 MBq, specific activity 2200 Ci/mmol), 50 μL of H_2O_2 (3%), and 50 μL of 1 N HCl in a sealed vial. The reaction was allowed to proceed at room temperature for 2 min and was terminated by addition of $NaHSO_3$. The reaction, after neutralization with sodium bicarbonate, was extracted with ethyl acetate. The extract was dried by passing through an anhydrous Na_2SO_4 column and was then blown dry with a stream of nitrogen gas. The radioiodinated ligand was purified by HPLC on a Cosmosil C_{18} column with an isocratic solvent of H_2O/acetonitrile (3:7) at a flow rate of 1.0 mL/min.

Binding Assays Using the Aggregated Aβ Peptide in Solution. A solid form of Aβ(1−42) was purchased from Peptide Institute (Osaka, Japan). Aggregation was carried out by gently dissolving the peptide (0.25 mg/mL) in a buffer solution (pH 7.4) containing 10 mM sodium phosphate and 1 mM EDTA. The solution was incubated at 37 °C for 42 h with gentle and constant shaking. (*Z*)-2-(4-Aminobenzylidene)-5-iodobenzofuran-3(2*H*)-one ([^{125}I]AAU) was synthesized and used as the radioligand for the competition binding experiments (K_d value of [^{125}I]AAU is 4.2 nM) (*19*). The binding experiments were carried out in 12 × 75 mm borosilicate glass tubes according to a procedure described previously (*19*). A mixture containing 50 μL of test compound (0.8 nM−12.5 μM in 10% ethanol), 50 μL of 0.02 nM [^{125}I]AAU, 50 μL of Aβ(1−42) aggregate, and 850 μL of 10% ethanol was incubated at room temperature for 3 h. The mixture was then filtered through Whatman GF/B filters using a Brandel M-24 cell harvester, and the filters containing the bound ^{125}I ligand were placed in a gamma counter. Values for the half-maximal inhibitory concentration (IC_{50}) were determined from displacement curves of three independent experiments using GraphPad *Prism* 4.0, and those for the inhibition constant (K_i) were calculated using the Cheng-Prusoff equation (*22*): $K_i = IC_{50}/(1 + [L]/K_d)$, where [L] is the concentration of [^{125}I]AAU used in the assay, and K_d is the dissociation constant of AAU (4.2 nM) (*19*).

Staining of Amyloid Plaques in Transgenic Mouse Brain Sections. Tg2576 transgenic mice (20 month of age) were used as an Alzheimer's model. The brain was removed and sliced into serial sections 10 μm thick. Each slide was incubated with a 50% ethanol solution of compound **9**, **14**, **15**, **16**, and **17** (100 μM). Finally, the sections were washed in 50% EtOH for 3 min two times. Fluorescent observation was performed with the Nikon system (Excitation filter, 450−490 nm; Dichroic mirror, DM505; Barrier filter, BA520). Thereafter, the serial sections were also stained with thioflavin S, a pathological dye commonly used for staining Aβ plaques in the brain.

In Vivo Biodistribution in Normal Mice. Animal studies were conducted in accordance with our institutional guidelines and were approved by Nagasaki University Animal Care Committee. A saline solution (100 μL) containing radiolabeled agents (4.2−6.3 kBq) and 10% ethanol was intravenously injected directly into the tail vein of ddY mice (5 weeks old, average weight 20−25 g). The mice were sacrificed at various time points postinjection. The organs of interest were removed and weighed, and the radioactivity was measured with an automatic gamma counter (Aloka, ARC-380). Percent dose per gram of samples was calculated by comparing the sample counts with the counts of the initial dose.

In Vitro Autoradiography. Postmortem brain tissues from an autopsy-confirmed case of AD (73-year-old male) and a control subject (36-year-old male) were obtained from BioChain Institute Inc. The presence and localization of plaques on the sections were confirmed with immunohistochemical staining using a monoclonal Aβ antibody BC05 (Wako) as reported (*23*). The sections were incubated with [^{125}I]**15** (120000 cpm/100 μL) for 1 h at room temperature. They were then dipped in saturated lithium carbonate in 40% EtOH (two 2-min washes) and washed with 40% EtOH (one 2-min wash), before being rinsed with water for 30 s. After drying, the ^{125}I-labeled sections were exposed to a Fuji Film imaging plate overnight.

RESULTS AND DISCUSSION

Chemistry. The target aurone derivatives (**9**, **14**, **15**, **16**, and **17**) were prepared as shown in Schemes 1−3. The synthesis of

Scheme 1

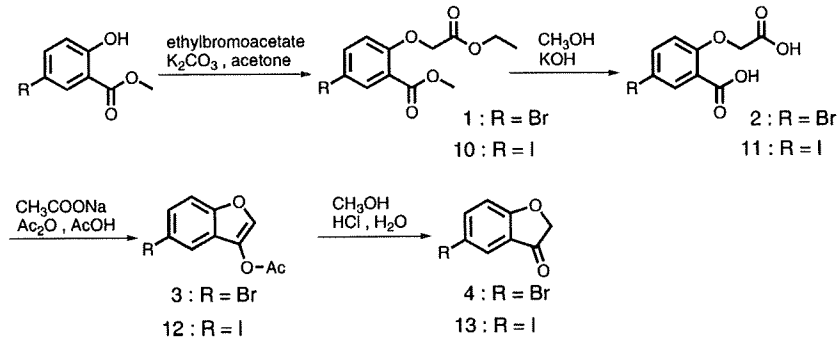

Scheme 2

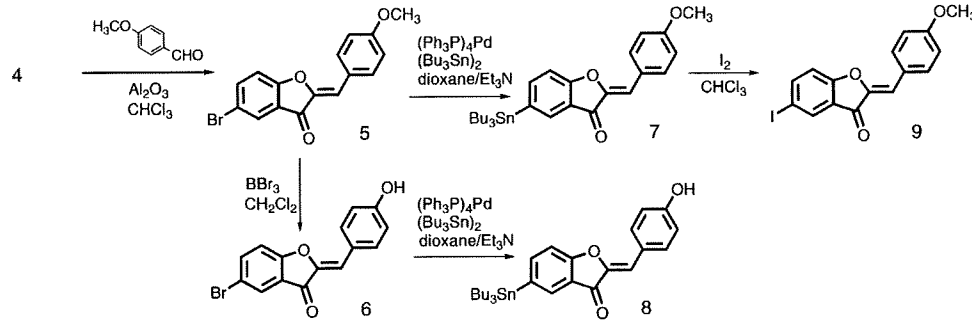

Scheme 3

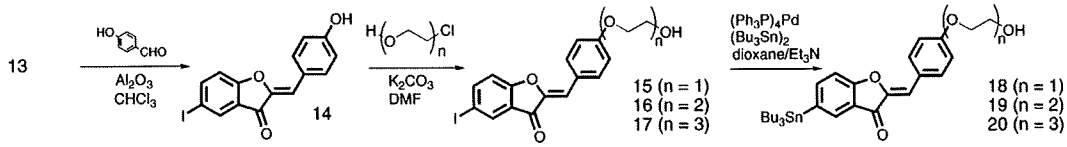

the aurone backbone was achieved by an Aldol reaction of benzofuranones with benzaldehydes using Al_2O_3 (*23*). In this process, benzofuranones were reacted with methoxy benzaldehyde or hydroxy benzaldehyde in the presence of Al_2O_3 in chloroform at room temperature to form compounds **5** and **14** in yields of 85.7% and 87.0%, respectively. Compound **5** was converted to **6** by demethylation with BBr_3 in CH_2Cl_2 (5.2% yields). Direct alkylation of **14** with ethylene chlorohydrin, ethylene glycol mono-2-chloroethyl ether, or 2-[2-(2-chloroethoxy)ethoxy]ethanol with potassium carbonate in DMF resulted in **15**, **16**, and **17**, respectively. The tributyltin derivatives (**7**, **8**, **18**, **19**, and **20**) were prepared from the corresponding compounds (**5**, **6**, **15**, **16**, and **17**) using a halogen to tributyltin exchange reaction catalyzed by Pd(0) for yields of 15.3%, 12.0%, 25.0%, 31.4%, and 30.3%, respectively. The tributyltin derivatives were used as the starting materials for radioiodination in the preparation of [^{125}I]**9**, [^{125}I]**14**, [^{125}I]**15**, [^{125}I]**16**, and [^{125}I]**17**. Novel radioiodinated aurones were achieved by an iododestannylation reaction using hydrogen peroxide as the oxidant, which produced the desired radioiodinated ligands (Scheme 4). It was anticipated that the no-carrier-added preparation would result in a final product bearing a theoretical specific activity similar to that of ^{125}I (2200 Ci/mmol). The radiochemical identities of the radioiodinated ligands were verified by coinjection with nonradioactive compounds by their HPLC profiles (Supporting Information). Five radioiodinated products were obtained in 25−57% radiochemical yields with radiochemical purities of >95% after purification by HPLC.

Binding Experiments Using Aβ Aggregates in Vitro. Our initial screening of the affinity of aurone derivatives (**9**, **14**, **15**, **16**, and **17**) was carried out with Aβ(1−42) aggregates, using

Scheme 4

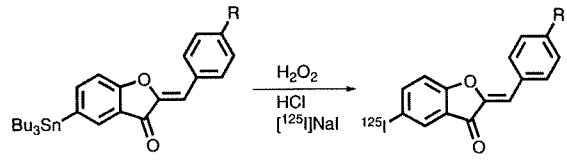

7
8
18
19
20

[^{125}I]9 (R = OCH_3)
[^{125}I]14 (R = OH)
[^{125}I]15 (R = OCH_2CH_2OH)
[^{125}I]16 (R = $(OCH_2CH_2)_2OH$)
[^{125}I]17 (R = $(OCH_2CH_2)_3OH$)

[^{125}I]AAU as the competing radioligand (Table 1). The K_i values estimated for **9**, **14**, **15**, **16**, and **17** were 2.9, 1.3, 1.1, 3.4, and 2.6 nM, respectively. These values suggested that the new series of aurone derivatives had binding affinity for Aβ(1−42) aggregates despite their substituted groups. The binding affinity is in the same range as that of aurone derivatives possessing a nucleophilic group (NH_2, NHMe, NMe_2), reported previously

Table 1. Inhibition Constants (K_i) of Newly Synthesized Aurone Derivatives for the Binding of Ligands to Aβ (1−42) Aggregates

compound	K_i (nM)[a]
9	2.89 ± 0.42
14	1.28 ± 0.29
15	1.05 ± 0.06
16	3.36 ± 0.29
17	2.56 ± 0.31

[a] Data are the mean ± SEM for two independent measurements done in triplicate.

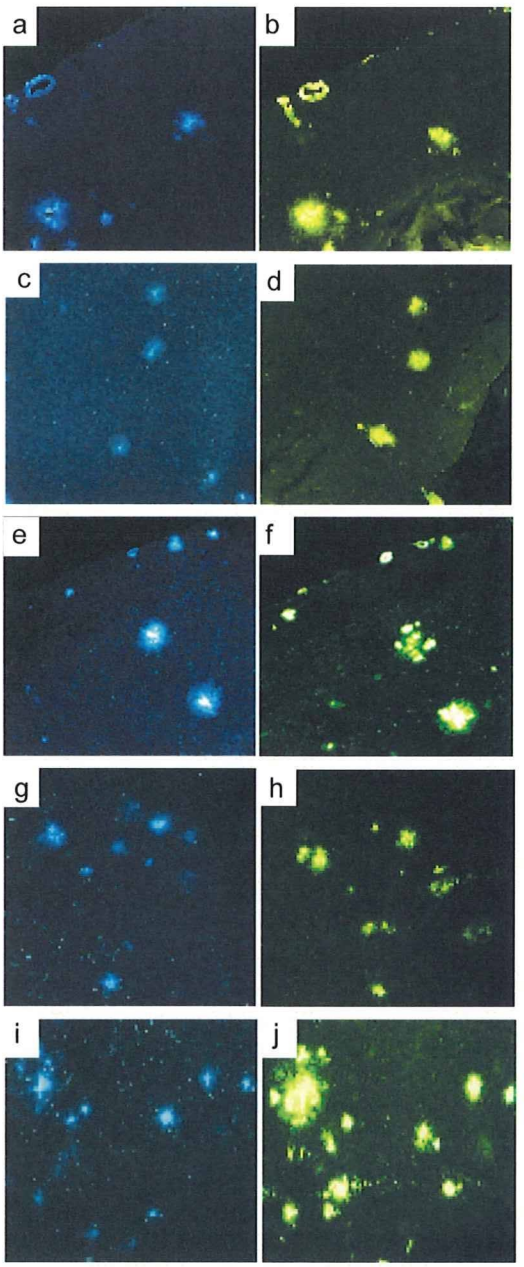

Figure 2. Neuropathological staining of **9**, **14**, **15**, **16**, and **17** (a, c, e, g, and i) in 10 μm sections from a mouse model of AD. Labeled plaques were confirmed by staining of the adjacent sections with thioflavin S (b, d, f, h, and j).

(*19*). These results clearly indicated that there exists considerable tolerance for structural modifications of aurone derivatives. The binding affinity of aurone derivatives is very close to that of known β-amyloid-imaging agents such as SB-13 (K_i = 1.2 nM) (*24*), PIB (K_i = 2.8 nM) (*25*), and IMPY (K_i = 1.4 nM) (*24*), indicating that they have strong enough affinity to test clinically.

Neuropathological Staining of Mouse Brain Sections. To confirm the affinity of aurone derivatives for β-amyloid plaques in the mouse brain, neuropathological fluorescent staining with **9**, **14**, **15**, **16**, and **17** was carried out using double transgenic Alzheimer's mouse brain sections (Figure 2). Many amyloid plaques were clearly stained with the derivatives, as reflected by the high binding affinity for Aβ aggregates in in vitro competition assays. The labeling pattern was consistent with that observed with thioflavin S. These results suggest that novel aurone derivatives show affinity for β-amyloid plaques in the mouse brain in addition to having binding affinity for synthetic Aβ42 aggregates.

Table 2. Biodistribution of Radioactivity after Injection of Aurone Derivatives in Normal Mice[a]

	time after injection (min)			
tissue	2	10	30	60
		[^{125}I]**9**		
blood	3.16 (0.82)	1.51 (0.23)	0.95 (0.19)	0.70 (0.60)
liver	6.87 (2.18)	5.16 (0.73)	2.76 (0.40)	1.86 (0.83)
kidney	7.26 (2.18)	7.00 (1.49)	4.93 (1.52)	2.43 (1.17)
intestine	1.59 (0.51)	4.70 (1.46)	11.67 (3.56)	9.02 (3.14)
spleen	1.45 (0.56)	0.74 (0.10)	0.48 (0.10)	0.43 (0.14)
pancreas	2.83 (0.75)	0.77 (0.17)	0.62 (0.75)	0.16 (0.05)
heart	3.84 (1.04)	1.06 (0.10)	0.37 (0.09)	0.25 (0.12)
stomach[b]	0.39 (0.20)	0.89 (0.48)	0.42 (0.13)	0.82 (0.46)
brain	1.69 (0.43)	0.54 (0.12)	0.11 (0.05)	0.03 (0.02)
		[^{125}I]**14**		
blood	3.14 (0.39)	2.77 (0.28)	1.75 (0.38)	0.87 (0.28)
liver	6.05 (1.49)	6.63 (1.08)	4.23 (0.63)	4.45 (3.14)
kidney	11.08 (2.96)	11.22 (2.26)	5.82 (1.11)	2.43 (1.04)
intestine	2.11 (0.75)	6.12 (0.83)	12.67 (2.13)	14.87 (5.42)
spleen	2.18 (0.48)	1.36 (0.83)	0.69 (0.14)	0.42 (0.02)
pancreas	5.28 (0.99)	2.65 (0.64)	0.92 (0.19)	0.36 (0.09)
heart	6.23 (0.63)	2.57 (0.41)	0.98 (0.14)	0.42 (0.14)
stomach[b]	0.93 (0.28)	1.46 (0.23)	1.22 (0.72)	1.89 (1.01)
brain	3.07 (0.39)	1.48 (0.19)	0.37 (0.07)	0.14 (0.12)
		[^{125}I]**15**		
blood	4.97 (0.96)	3.88 (1.09)	2.38 (0.85)	1.24 (0.35)
liver	13.4 (3.20)	13.3 (2.59)	7.60 (1.95)	5.27 (0.64)
kidney	11.3 (1.23)	10.8 (2.58)	6.09 (2.43)	2.50 (1.30)
intestine	2.78 (0.42)	7.83 (2.22)	17.82 (3.58)	20.93 (4.46)
spleen	2.72 (0.28)	1.02 (0.22)	0.50 (0.13)	0.21 (0.09)
pancreas	6.38 (0.63)	1.61 (0.61)	0.59 (0.21)	0.29(0.15)
heart	6.30 (0.65)	2.30 (0.46)	0.83 (0.15)	0.72 (0.58)
stomach[b]	1.88 (0.41)	3.23 (2.58)	5.15 (4.43)	1.45 (0.78)
brain	4.51 (0.25)	1.48 (0.28)	0.24 (0.03)	0.09 (0.04)
		[^{125}I]**16**		
blood	3.61 (0.74)	5.18 (2.54)	1.11 (0.73)	0.68 (0.45)
liver	12.5 (3.21)	11.6 (1.75)	9.31 (2.66)	7.12 (4.05)
kidney	12.0 (0.99)	10.3 (1.17)	5.75 (1.53)	2.55 (1.12)
intestine	2.35 (1.33)	8.18 (2.32)	19.7 (7.86)	26.38 (5.95)
spleen	2.26 (0.53)	1.56 (0.45)	0.78 (0.26)	0.45 (0.21)
pancreas	5.67(2.72)	2.24 (0.68)	1.40 (0.44)	0.39 (0.29)
heart	6.04 (0.38)	2.77 (0.94)	1.21 (0.66)	0.66 (0.57)
stomach[b]	1.71 (0.38)	5.65 (6.63)	5.00 (2.83)	6.58 (4.59)
brain	3.69 (0.22)	1.53 (0.31)	0.38 (0.05)	0.16 (0.03)
		[^{125}I]**17**		
blood	2.98 (0.64)	4.62 (2.17)	0.83 (0.64)	0.51 (0.31)
liver	12.95 (3.43)	11.20 (1.51)	8.34 (1.98)	7.70 (3.93)
kidney	11.58 (1.13)	9.66 (2.28)	5.84 (1.79)	2.41 (1.22)
intestine	2.52 (0.39)	7.50 (4.85)	17.95 (7.53)	22.64 (5.89)
spleen	2.26 (0.65)	1.40 (0.23)	0.84 (0.23)	0.56 (0.24)
pancreas	5.51 (0.59)	1.84 (0.44)	0.87 (0.37)	0.79 (0.70)
heart	5.67 (1.02)	2.24 (0.56)	1.40 (0.49)	0.39 (0.68)
stomach[b]	3.29 (1.47)	4.73 (5.14)	7.45 (4.62)	7.61 (5.20)
brain	2.81 (0.19)	2.32 (0.21)	0.18 (0.06)	0.08 (0.04)

[a] Expressed as % injected dose per gram. Each value represents the mean (SD) for 4−5 animals. [b] Expressed as % injected dose per organ.

Biodistribution Experiments. To evaluate brain uptake of the aurone derivatives, biodistribution experiments were performed in normal mice with five radioiodinated aurones ([^{125}I]**9**, [^{125}I]**14**, [^{125}I]**15**, [^{125}I]**16**, and [^{125}I]**17**) (Table 2). Radioactivity after injection of the aurone derivatives penetrated the blood−brain barrier showing excellent uptake ranging from 1.7% to 4.5% ID/g brain at 2 min postinjection, a level sufficient for imaging β-amyloid plaques in the brain. In addition, it displayed good clearance from the normal brain with 0.1−0.4% ID/g at 30 min postinjection. Since normal mice were used for the biodistribution experiments, no Aβ plaques were expected in the young mice; therefore, the washout of probes from the brain should be rapid to obtain a higher signal-to-noise ratio earlier in the AD brain. One way to select a ligand with

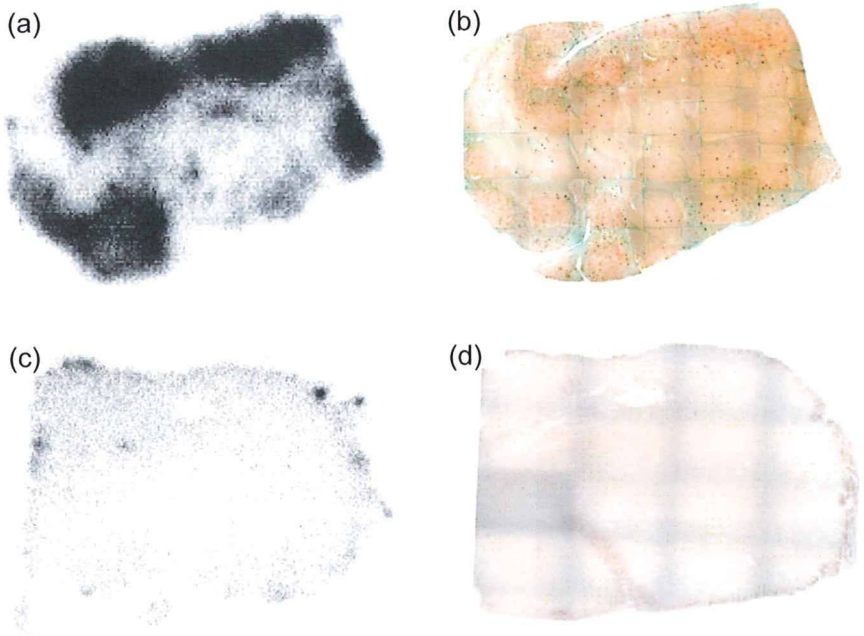

Figure 3. In vitro ARG of [^{125}I]**15** reveals a distinct labeling of amyloid plaques in AD brain sections (a). Under similar conditions, there is very little labeling of [^{125}I]**15** in control brain section (c). The presence and localization of plaques in the sections were confirmed with immunohistochemical staining using a monoclonal Aβ antibody (b, d).

appropriate in vivo kinetics is to use brain$_{2min}$/brain$_{30min}$ as an index to compare the washout rate. The five radioiodinated aurone derivatives [^{125}I]**9**, [^{125}I]**14**, [^{125}I]**15**, [^{125}I]**16**, and [^{125}I]**17** showed brain$_{2min}$/brain$_{30min}$ ratios of 15.4, 8.3, 18.8, 9.7, and 15.6, respectively. [^{125}I]**15** had the best washout index. Previously reported radioiodinated aurones showed high uptake (1.9−4.6% ID/g at 2 min postinjection) and good clearance from the brain (0.3−0.5% ID/g at 30 min postinjection) (*19*). However, the brain$_{2min}$/brain$_{30min}$ ratios of these compounds were 7.3−9.9, lower than that of [^{125}I]**15**, indicating that [^{125}I]**15** could clear more rapidly from the normal mouse brain than aurones with amino groups. It has been reported that [^{123}I]IMPY entered the brain rapidly (2.88% ID at 2 min postinjection) and was cleared from normal brain (0.26% ID at 30 min postinjection), indicating the brain$_{2min}$/brain$_{30min}$ ratio to be 11.1 (*16*). The aurone derivatives reported in this study appear superior to IMPY in pharmacokinetics, in addition to showing similar binding affinities sufficient for the imaging of β-amyloid plaques in vivo. The pharmacokinetics demonstrated by [^{125}I]**15** is critical to the detection of β-amyloid plaques in the AD brain.

In Vitro Autoradiography. Next, [^{125}I]**15** was investigated for its binding affinity for β-amyloid plaques by in vitro autoradiography in human AD brain sections as shown in Figure 3. Autoradiographic images of [^{125}I]**15** showed high levels of radioactivity in the brain sections (Figure 3a). Furthermore, we confirmed that the hot spots of [^{125}I]**15** corresponded with those of in vitro immunohistochemical staining in the same brain sections (Figure 3b). In contrast, normal human brain displayed no remarkable accumulation of [^{125}I]**15** (Figure 3c), correlating well with the absence of β-amyloid plaques (Figure 3d). These results demonstrate the feasibility of using [^{125}I]**15** as a probe for detecting β-amyloid plaques in the brains of AD patients with SPECT.

CONCLUSION

In conclusion, we successfully designed and synthesized a new series of aurone derivatives as amyloid-imaging agents with high affinity for Aβ(1−42) aggregates in vitro. The derivatives clearly stained amyloid plaques in an animal model of AD, reflecting strong binding to Aβ aggregates in vitro. In biodistribution experiments using normal mice, they displayed good penetration of and fast washout from the brain, especially [^{125}I]**15**. A specific plaque-labeling signal was clearly depicted by [^{125}I]**15** in postmortem AD brain sections. Taken together, the present results suggest [^{125}I]**15** to be a potentially useful probe for the SPECT-based imaging of β-amyloid plaques.

ACKNOWLEDGMENT

This work was supported in part by the Industrial Technology Research Grant Program in 2005 from the New Energy and Industrial Technology Development Organization (NEDO) of Japan and the Program for Promotion of Fundamental Studies in Health Sciences of the National Institute of Biomedical Innovation (NIBIO).

Supporting Information Available: HPLC data of compounds **9**, **14**, **15**, **16**, and **17**. This material is available free of charge via the Internet at http://pubs.acs.org.

LITERATURE CITED

(1) Klunk, W. E. (1998) Biological markers of Alzheimer's disease. *Neurobiol. Aging 19*, 145–7.
(2) Selkoe, D. J. (2001) Alzheimer's disease: genes, proteins, and therapy. *Physiol. Rev. 81*, 741–66.
(3) Selkoe, D. J. (2000) Imaging Alzheimer's amyloid. *Nat. Biotechnol. 18*, 823–4.
(4) Mathis, C. A., Wang, Y., and Klunk, W. E. (2004) Imaging β-amyloid plaques and neurofibrillary tangles in the aging human brain. *Curr. Pharm. Des. 10*, 1469–92.
(5) Nordberg, A. (2004) PET imaging of amyloid in Alzheimer's disease. *Lancet Neurol. 3*, 519–27.
(6) Mathis, C. A., Wang, Y., Holt, D. P., Huang, G. F., Debnath, M. L., and Klunk, W. E. (2003) Synthesis and evaluation of ^{11}C-labeled 6-substituted 2-arylbenzothiazoles as amyloid imaging agents. *J. Med. Chem. 46*, 2740–54.
(7) Klunk, W. E., Engler, H., Nordberg, A., Wang, Y., Blomqvist, G., Holt, D. P., Bergstrom, M., Savitcheva, I., Huang, G. F., Estrada, S., Ausen, B., Debnath, M. L., Barletta, J., Price, J. C., Sandell, J., Lopresti, B. J., Wall, A., Koivisto, P., Antoni, G., Mathis, C. A., and Langstrom, B. (2004) Imaging brain amyloid

in Alzheimer's disease with Pittsburgh compound-B. *Ann. Neurol. 55*, 306–19.

(8) Ono, M., Wilson, A., Nobrega, J., Westaway, D., Verhoeff, P., Zhuang, Z. P., Kung, M. P., and Kung, H. F. (2003) ^{11}C-labeled stilbene derivatives as Aβ-aggregate-specific PET imaging agents for Alzheimer's disease. *Nucl. Med. Biol. 30*, 565–71.

(9) Verhoeff, N. P., Wilson, A. A., Takeshita, S., Trop, L., Hussey, D., Singh, K., Kung, H. F., Kung, M. P., and Houle, S. (2004) In-vivo imaging of Alzheimer disease β-amyloid with [^{11}C]SB-13 PET. *Am. J. Geriatr. Psychiatry 12*, 584–95.

(10) Rowe, C. C., Ackerman, U., Browne, W., Mulligan, R., Pike, K. L., O'Keefe, G., Tochon-Danguy, H., Chan, G., Berlangieri, S. U., Jones, G., Dickinson-Rowe, K. L., Kung, H. P., Zhang, W., Kung, M. P., Skovronsky, D., Dyrks, T., Holl, G., Krause, S., Friebe, M., Lehman, L., Lindemann, S., Dinkelborg, L. M., Masters, C. L., and Villemagne, V. L. (2008) Imaging of amyloid beta in Alzheimer's disease with ^{18}F-BAY94-9172, a novel PET tracer: proof of mechanism. *Lancet Neurol. 7*, 129–35.

(11) Kudo, Y., Okamura, N., Furumoto, S., Tashiro, M., Furukawa, K., Maruyama, M., Itoh, M., Iwata, R., Yanai, K., and Arai, H. (2007) 2-(2-[2-Dimethylaminothiazol-5-yl]ethenyl)-6-(2-[fluoro]ethoxy)benzoxazole: A novel PET agent for in vivo detection of dense amyloid plaques in Alzheimer's disease patients. *J. Nucl. Med. 48*, 553–561.

(12) Agdeppa, E. D., Kepe, V., Liu, J., Flores-Torres, S., Satyamurthy, N., Petric, A., Cole, G. M., Small, G. W., Huang, S. C., and Barrio, J. R. (2001) Binding characteristics of radiofluorinated 6-dialkylamino-2-naphthylethylidene derivatives as positron emission tomography imaging probes for β-amyloid plaques in Alzheimer's disease. *J. Neurosci. 21*, RC189.

(13) Shoghi-Jadid, K., Small, G. W., Agdeppa, E. D., Kepe, V., Ercoli, L. M., Siddarth, P., Read, S., Satyamurthy, N., Petric, A., Huang, S. C., and Barrio, J. R. (2002) Localization of neurofibrillary tangles and β-amyloid plaques in the brains of living patients with Alzheimer disease. *Am. J. Geriatr. Psychiatry 10*, 24–35.

(14) Small, G. W., Kepe, V., Ercoli, L. M., Siddarth, P., Bookheimer, S. Y., Miller, K. J., Lavretsky, H., Burggren, A. C., Cole, G. M., Vinters, H. V., Thompson, P. M., Huang, S. C., Satyamurthy, N., Phelps, M. E., and Barrio, J. R. (2006) PET of brain amyloid and tau in mild cognitive impairment. *N. Engl. J. Med. 355*, 2652–63.

(15) Kung, M. P., Hou, C., Zhuang, Z. P., Zhang, B., Skovronsky, D., Trojanowski, J. Q., Lee, V. M., and Kung, H. F. (2002) IMPY: an improved thioflavin-T derivative for in vivo labeling of beta-amyloid plaques. *Brain Res. 956*, 202–10.

(16) Zhuang, Z. P., Kung, M. P., Wilson, A., Lee, C. W., Plossl, K., Hou, C., Holtzman, D. M., and Kung, H. F. (2003) Structure-activity relationship of imidazo[1,2-a]pyridines as ligands for detecting β-amyloid plaques in the brain. *J. Med. Chem. 46*, 237–43.

(17) Newberg, A. B., Wintering, N. A., Plossl, K., Hochold, J., Stabin, M. G., Watson, M., Skovronsky, D., Clark, C. M., Kung, M. P., and Kung, H. F. (2006) Safety, biodistribution, and dosimetry of ^{123}I-IMPY: a novel amyloid plaque-imaging agent for the diagnosis of Alzheimer's disease. *J. Nucl. Med. 47*, 748–54.

(18) Newberg, A. B., Wintering, N. A., Clark, C. M., Plossl, K., Skovronsky, D., Seibyl, J. P., Kung, M. P., and Kung, H. F. (2006) Use of ^{123}I IMPY SPECT to differentiate Alzheimer's disease from controls. *J. Nucl. Med. 47*, 78P.

(19) Ono, M., Maya, Y., Haratake, M., Ito, K., Mori, H., and Nakayama, M. (2007) Aurones serve as probes of β-amyloid plaques in Alzheimer's disease. *Biochem. Biophys. Res. Commun. 361*, 116–21.

(20) Roberts, M., Bentley, M., and Harris, J. (2002) Chemistry for peptide and protein PEGylation. *Adv. Drug Delivery Rev. 54*, 459–76.

(21) Harris, J., and Chess, R. (2003) Effect of pegylation on pharmaceuticals. *Nat. Rev. Drug Discovery 2*, 214–21.

(22) Cheng, Y., and Prusoff, W. (1973) Relationship between the inhibition constant (K1) and the concentration of inhibitor which causes 50% inhibition (I50) of an enzymatic reaction. *Biochem. Pharmacol.* 3099–3108.

(23) Bryant, W., and Huhn, G. (1995) A practical preparation of 7-methoxy-3(2H)-benzofuranone. *Synth. Commun. 25*, 915–20.

(24) Kung, M. P., Hou, C., Zhuang, Z. P., Skovronsky, D., and Kung, H. F. (2004) Binding of two potential imaging agents targeting amyloid plaques in postmortem brain tissues of patients with Alzheimer's disease. *Brain Res. 1025*, 98–105.

(25) Zhang, W., Oya, S., Kung, M. P., Hou, C., Maier, D. L., and Kung, H. F. (2005) F-18 stilbenes as PET imaging agents for detecting β-amyloid plaques in the brain. *J. Med. Chem. 48*, 5980–8.

BC8003292

Eur J Nucl Med Mol Imaging (2010) 37:377–385
DOI 10.1007/s00259-009-1262-2

ORIGINAL ARTICLE

Quantification of regional myocardial oxygen metabolism in normal pigs using positron emission tomography with injectable ^{15}O-O_2

Takashi Temma · Hidehiro Iida · Takuya Hayashi · Noboru Teramoto · Youichiro Ohta · Nobuyuki Kudomi · Hiroshi Watabe · Hideo Saji · Yasuhiro Magata

Received: 27 April 2009 / Accepted: 10 August 2009 / Published online: 4 September 2009

Abstract
Purpose Although ^{15}O-O_2 gas inhalation can provide a reliable and accurate myocardial metabolic rate for oxygen by PET, the spillover from gas volume in the lung distorts the images. Recently, we developed an injectable method in which blood takes up ^{15}O-O_2 from an artificial lung, and this made it possible to estimate oxygen metabolism without the inhalation protocol. In the present study, we evaluated the effectiveness of the injectable ^{15}O-O_2 system in porcine hearts.
Methods PET scans were performed after bolus injection and continuous infusion of injectable ^{15}O-O_2 via a shunt between the femoral artery and the vein in normal pigs. The injection method was compared to the inhalation method. The oxygen extraction fraction (OEF) in the lateral walls of the heart was calculated by a compartmental model in view of the spillover and partial volume effect.
Results A significant decrease of lung radioactivity in PET images was observed compared to the continuous inhalation of ^{15}O-O_2 gas. Furthermore, the injectable ^{15}O-O_2 system provides a measurement of OEF in lateral walls of the heart that is similar to the continuous-inhalation method (0.71 ± 0.036 and 0.72 ± 0.020 for the bolus-injection and continuous-infusion methods, respectively).
Conclusion These results indicate that injectable ^{15}O-O_2 has the potential to evaluate myocardial oxygen metabolism.

Keywords Myocardial oxygen metabolism · PET · Pig · OEF · Injectable ^{15}O-O_2

T. Temma · H. Saji
Department of Patho-Functional Bioanalysis,
Graduate School of Pharmaceutical Sciences, Kyoto University,
Kyoto, Japan

H. Iida · T. Hayashi · N. Teramoto · Y. Ohta · N. Kudomi · H. Watabe
Department of Investigative Radiology,
National Cardiovascular Center Research Institute,
Osaka, Japan

Y. Magata (✉)
Laboratory of Genome Bio-Photonics,
Photon Medical Research Center,
Hamamatsu University School of Medicine,
1-20-1 Handayama,
Hamamatsu 431-3192, Japan
e-mail: magata@hama-med.ac.jp

Introduction

In the myocardium, fatty acid or glucose is used to produce energy by aerobic metabolism. Oxygen is one of the most important substrates closely related to the aerobic metabolism in the TCA cycle; thus, oxygen metabolism should be a direct reflection of myocardial metabolism of these substrates. Therefore, there has been considerable interest in the development of a method to quantify oxygen metabolism in the myocardium.

Recently, ^{11}C-acetate has been used for this purpose [1–5]. ^{11}C-acetate is taken up by the mitochondria and metabolically converted into acetyl-CoA. It then enters the TCA cycle and is transformed to ^{11}C-CO_2, which is cleared rapidly from the myocardium. Thus, the clearance pharmacokinetics reflects oxygen metabolism in the myocardium. However, the quantification of oxygen metabolism using ^{11}C-acetate is quite difficult because of various intermediary compounds.

The use of ^{15}O-O_2 gas inhalation and PET scanning can provide a quantitative myocardial metabolic rate for oxygen ($MMRO_2$) [6, 7]. The tracer kinetic model used is based on that originally proposed to describe the behavior of ^{15}O-O_2 in brain tissue [8, 9]. However, the direct translation of the

compartmental model for the brain to the heart is not permitted, because subtraction for spillover from gas volume in addition to that from the blood pool is needed. A previous study demonstrated that the gas volume can be accurately estimated from the transmission scan data; thus, this technique did not require additional emission scanning for estimating the quantitative gas volume images [6, 7]. However, gaseous radioactivity in the lung during the inhalation of ^{15}O-O_2 gas is too high in comparison to other regions. Subtraction for this contribution is straightforward and accurate using the transmission scan-derived gaseous volume images, but the lung radioactivity degraded image quality in the estimated $MMRO_2$ images.

As an alternative to gas inhalation, we recently developed a method to prepare an injectable form of ^{15}O-O_2. This was accomplished by exposing pre-collected blood to ^{15}O-O_2 gas using a small artificial lung system resulting in a maximum yield of 130 MBq/ml. We demonstrated that cerebral oxygen metabolism could be estimated in normal and ischemic rats using injectable ^{15}O-O_2 [10–12]. This technique has the potential of avoiding the inhalation protocol.

The aim of the present study was therefore to test the feasibility of using the injectable ^{15}O-O_2 oxygen system for estimating myocardial oxygen metabolism in pigs. The injection method was compared to the inhalation method to determine if the injection method resulted in a reduction of lung radioactivity, an improved image quality, a more accurate estimate of myocardial oxygen metabolism, and an improved signal-to-noise ratio.

Materials and methods

Theory

^{15}O-Oxygen was administered by IV injection or inhalation and was carried as ^{15}O-hemoglobin by blood to peripheral tissues including the myocardium, where it was converted to ^{15}O-water (^{15}O-H_2O_{met}) through aerobic metabolism. The increased distribution volume of ^{15}O-H_2O_{met}, represented by the exchangeable water space of tissue, causes delayed removal of radioactivity. This allows the definition of an appropriate model and equations to be derived for the calculation of a regional myocardial metabolic rate for oxygen ($rMMOR_2$) and regional oxygen extraction fraction (rOEF). Previous studies demonstrated that these calculations were similar to those used for estimating cerebral blood flow and oxygen metabolism and require the measurement of regional myocardial blood flow (rMBF) and a correction for spillover of activity from the vascular pools and the pulmonary alveoli [6, 7]. rMBF was measured by the ^{15}O-H_2O injection technique [13]. Activity in the vascular pools of the heart chambers and the lung was evaluated with a conventional measurement of blood volume using ^{15}O-CO, and activity in the pulmonary alveoli was evaluated with an unconventional and indirect measurement of gas volume obtained from the transmission scan. Furthermore, the existence of recirculating ^{15}O-H_2O_{met} in the blood freely accessible to the myocardium was taken into consideration.

The differential equation describing the myocardial kinetics after administration of ^{15}O-O_2 can be written as follows:

$$\frac{dC^{myo}(t)}{dt} = OEF \cdot f \cdot A_o(t) + f \cdot A_w(t) - \left(\frac{f}{p} + \lambda\right) C^{myo}(t) \quad (1)$$

where $C^{myo}(t)$ designates the true radioactivity concentration in the myocardium at time t, f is myocardial blood flow, $A_O(t)$ is the ^{15}O-O_2 radioactivity concentration in arterial blood, $A_W(t)$ is the ^{15}O-H_2O radioactivity concentration in arterial blood, p is the myocardium/blood partition coefficient of water, and λ is the physical decay constant of O-15.

Solving Eq. (1) in terms of $C^{myo}(t)$ gives:

$$C^{myo}(t) = OEF \cdot f \cdot A_o(t) * e^{-\left(\frac{f}{p}+\lambda\right)\cdot t} + f \cdot A_w(t) * e^{-\left(\frac{f}{p}+\lambda\right)\cdot t} \quad (2)$$

where the asterisk denotes the convolution integral. During steady-state conditions under the continuous administration of ^{15}O-O_2, the following relationship holds:

$$C^{myo} = \frac{OEF \cdot f \cdot A_o + f \cdot A_w}{\left(\frac{f}{p} + \lambda\right)} \quad (3)$$

In the actual PET studies, the spillover from vascular pools and pulmonary alveoli and the partial volume effect should be taken into consideration [14]. Then, the measured radioactivity concentration in the region of interest (ROI) in the myocardium ($R^{myo}(t)$) can be expressed as:

$$\begin{aligned} R^{myo}(t) = {} & \alpha \cdot C^{myo}(t) \\ & + (V_B^{myo} \cdot A_t(t) - \alpha \cdot F_{Vein} \cdot OEF \cdot A_o(t) - \alpha \cdot F_{Vein} \cdot A_w(t)) \\ & + V_G^{myo} \cdot C_{gas}(t) \end{aligned} \quad (4)$$

where α denotes the myocardial tissue fraction, V_B^{myo} is the myocardial blood volume, $A_t(t)$ is the total O-15 radioactivity concentration in arterial blood, F_{vein} is the microscopic venous blood volume, V_G^{myo} is the gas volume in the myocardial ROI and $C_{gas}(t)$ is the O-15 radioactivity concentration in V_G^{myo}.

With the bolus injection or infusion methods using an artificial lung system, the radioactivity in the pulmonary alveoli is expected to be negligible in comparison with the inhalation method. Thus, Eq. (4) can be converted to:

$$R^{myo}(t) = \alpha \cdot C^{myo}(t) + (V_B^{myo} \cdot A_t(t) - \alpha \cdot F_{Vein} \cdot OEF \cdot A_o(t) - \alpha \cdot F_{Vein} \cdot A_w(t)) \quad (5)$$

Subjects

In this study, four healthy miniature pigs (22–30 kg) were used. The pigs were anesthetized by IM injection of ketamine and xylazine followed by continuous infusion of propofol (5 mg/kg/h). The animals were then placed in the supine position on the bed of the PET scanner. All experimental procedures were approved by the local animal welfare committee.

Injectable ^{15}O-O_2 preparation

In the "injection" study, injectable ^{15}O-O_2 was used. Injectable ^{15}O-O_2 was prepared as described previously [10–12]. In brief, part of an infusion line kit (Terumo Corporation, Tokyo, Japan) and an artificial lung 18 cm in length (Senko Medical Instrument Mfg Co. Ltd., Tokyo, Japan) were connected using silicone tubing to make a closed system. Then, venous blood collected from a pig, which was used in the following PET studies, was added to the system and circulated (100 ml/min) by a peristaltic pump, followed by introduction of ^{15}O–O_2 gas (~7,000 MBq/min/433 ml) into the artificial lung for 15 min to prepare injectable ^{15}O-O_2 (5.6–60.7 MBq/ml).

In the "continuous infusion" study, the left femoral artery and right femoral vein were both cannulated. The two cannulas from the artery and the vein were connected to the opposite sides of an artificial lung to create a femoral shunt. The blood flow in the shunt was aided by a peristaltic pump (30–50 ml/min). ^{15}O-O_2 gas (~7,000 MBq/min/433 ml) was continuously introduced into the artificial lung.

PET protocol (Fig. 1)

The PET scanner was an ECAT EXACT HR (CTI/Siemens) [15], which has an imaging field of view (FOV) of 55 cm in diameter and 15 cm in axial length. The spatial resolution of the scanner is 5.8 mm in full width at half maximum at the center of the FOV.

After obtaining a 20-min transmission scan for attenuation correction and gas volume estimation, the blood pool image was obtained with a 4-min PET scan after the pigs inhaled 2.7 GBq ^{15}O-CO for 30 s. Arterial blood samples were taken every minute during the ^{15}O-CO scanning, and

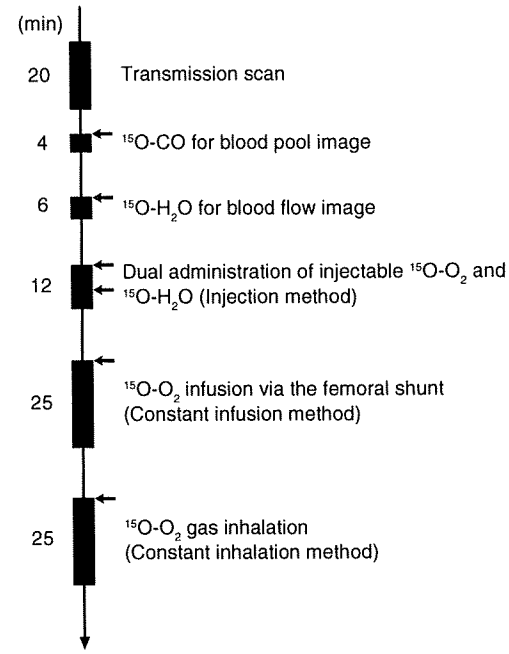

Fig. 1 Outline of the PET imaging study. The interval between scans was more than 15 min to allow for physical decay of O-15 radioactivity to background levels

the radioactivity concentration in the whole blood was measured with a NaI well-type scintillation counter calibrated against the PET scanner. Subsequently, ^{15}O-water was injected into the right femoral vein for 30 s at an infusion rate of 10 ml/min (injected radioactivity was about 1.11 GBq). Immediately after injection of ^{15}O-water, 26 dynamic frames (12×5 s, 8×15 s and 6×30 s) of PET data were acquired for 6 min.

Furthermore, two PET scans were successively performed after the IV injection of ^{15}O-O_2 (5.6–60.7 MBq/ml) for 30 s at an injection rate of 20–80 ml/min for the "injection" study, and by the continuous ^{15}O-O_2 gas infusion through the artificial lung in the femoral shunt for the "continuous infusion" study. In the "injection" study, 52 dynamic frames (12×5 s, 8×15 s, 6×30 s, 12×5 s, 8×15 s and 6×30 s) of PET data were acquired for 12 min, and 1.11 GBq of ^{15}O-water was injected IV for 30 s at 10 ml/min starting at 6 min after the administration of IV ^{15}O-O_2 according to the dual administration protocol we developed previously [16]. In the "continuous infusion" study, 26 dynamic frames (10×30 s, 5×60 s, 1×600 s and 10×30 s) were acquired for 25 min, and the 600-s frame was used for steady-state analysis.

Another PET scan was performed by ^{15}O-O_2 gas inhalation in one of the four pigs in the same protocol as the "continuous infusion" study. This was the "continuous inhalation" study. The interval between scans was more

than 15 min to allow for physical decay of O-15 radioactivity to background levels. All acquisitions were obtained in the two-dimensional mode (septa extended).

Data analysis

A filtered back-projection algorithm with a 6-mm Gaussian filter was used for image reconstruction. The reconstructed images had a matrix size of 128 × 128 × 47 and a voxel size of 1.84 × 1.84 × 3.38 mm, and all image data sets were resliced into short-axis images across the left ventricle [13].

Myocardial blood flow

rMBF was calculated from the injection of ^{15}O-H_2O by fitting the myocardial and arterial time-activity curve data to a single-tissue-compartment model that implemented corrections for partial-volume effects by introducing the tissue fraction. In addition, the model was corrected for spillover from the left ventricular (LV) chamber into the myocardial ROI by introducing the arterial blood volume [13]. In these experiments, the time-activity curves generated from large ROIs placed in the LV chamber were used as the input function.

Regional oxygen extraction fraction

In the "injection" study, rOEF was calculated according to Eqs. (2) and (5). In these formulations, F_{vein} was assumed to be 0.10 ml/g tissue and p was fixed at 0.90 ml/g. The blood volume image obtained from the ^{15}O-CO scan was used for the determination of V_B^{myo}. The value of $A_t(t)$ was obtained from the LV radioactivity concentration measured from the PET data set with small LV ROIs to minimize spillover from the myocardium. The calculation for the estimation of recirculating ^{15}O-H_2O was performed as previously described [16]. For the "continuous infusion" and "continuous inhalation" studies, in which a 600-s frame was regarded as steady-state, Eqs. (3) and (5) or Eqs. (3) and (4) were used for calculating rOEF, respectively.

Results

Table 1 summarizes the conditions of animals during the PET studies. The parameters were all within the physiologic range.

Figure 2 demonstrates the dynamic images obtained in the "injection", "continuous infusion", and "continuous inhalation" studies. With the injection and continuous-infusion methods, the right ventricle on the left side and the vena cava on the lower side were well delineated, whereas the left ventricle was moderately shown on the right side. The 16th frame (600~1,200 s after the initiation), which was used for steady-state analysis with the continuous-infusion method, was visibly distinct compared with all of the frames obtained with the injection method. However, with the continuous-inhalation method, neither ventricle could be depicted because of high radioactivity in the lung on the right and lower-side images.

The radioactivity in the blood pool obtained by ^{15}O-CO PET (Fig. 3g) and the gaseous volume estimated by inverse transmission data (Fig. 3h) were subtracted from the raw PET images (16th frame) with the continuous-inhalation and continuous-infusion methods, respectively (Fig. 3c and f). Both methods clearly delineated the myocardium after subtraction in comparison to the blood flow image (Fig. 3i). However, the continuous-inhalation method showed salient radioactivity on the lateral wall (Fig. 3c), whereas the continuous-infusion method showed only modest radioactivity in the myocardium (Fig. 3f). It is also notable that there was considerable radioactivity in the right ventricle with the continuous-infusion method even after the subtraction (Fig. 3f).

To further examine the differences between the continuous-infusion and continuous-inhalation methods, time-radioactivity curves during the PET scans were taken from four ROIs: the left ventricle (LV), right ventricle (RV), myocardium (Myo), and lung (Fig. 4). At the steady-state frame (600~1,200 s), the continuous-infusion method showed higher radioactivity in the RV and LV than in the myocardium (Fig. 4a), whereas the radioactivity of these regions was similar with the continuous-inhalation method (Fig. 4b). The radioactivity in LV was about two-thirds of that in RV in Fig. 4a, indicating that measurable radioactivity was excreted through the lung even after the femoral administration of ^{15}O-O_2. The lung excretion was also observed on the blood-subtracted image (Fig. 3e). Actually, there was significant radioactivity in the lung (Fig. 4a), although that was the lowest among the four ROIs. In contrast, the radioactivity in the myocardium was the lowest among the four ROIs with the continuous-inhalation method

Table 1 Physiological parameters of pigs during the PET studies

	pH	pCO_2 (mmHg)	pO_2 (mmHg)	tHb (g/dl)	O_2Sat (%)	HR (bpm)	BP (mmHg)	
							Diastolic	Systolic
Average	7.46	40.3	125.8	12.8	97.7	85	97.8	125.2
SD	0.032	2.51	16.69	1.30	1.83	19.5	10.4	19.3

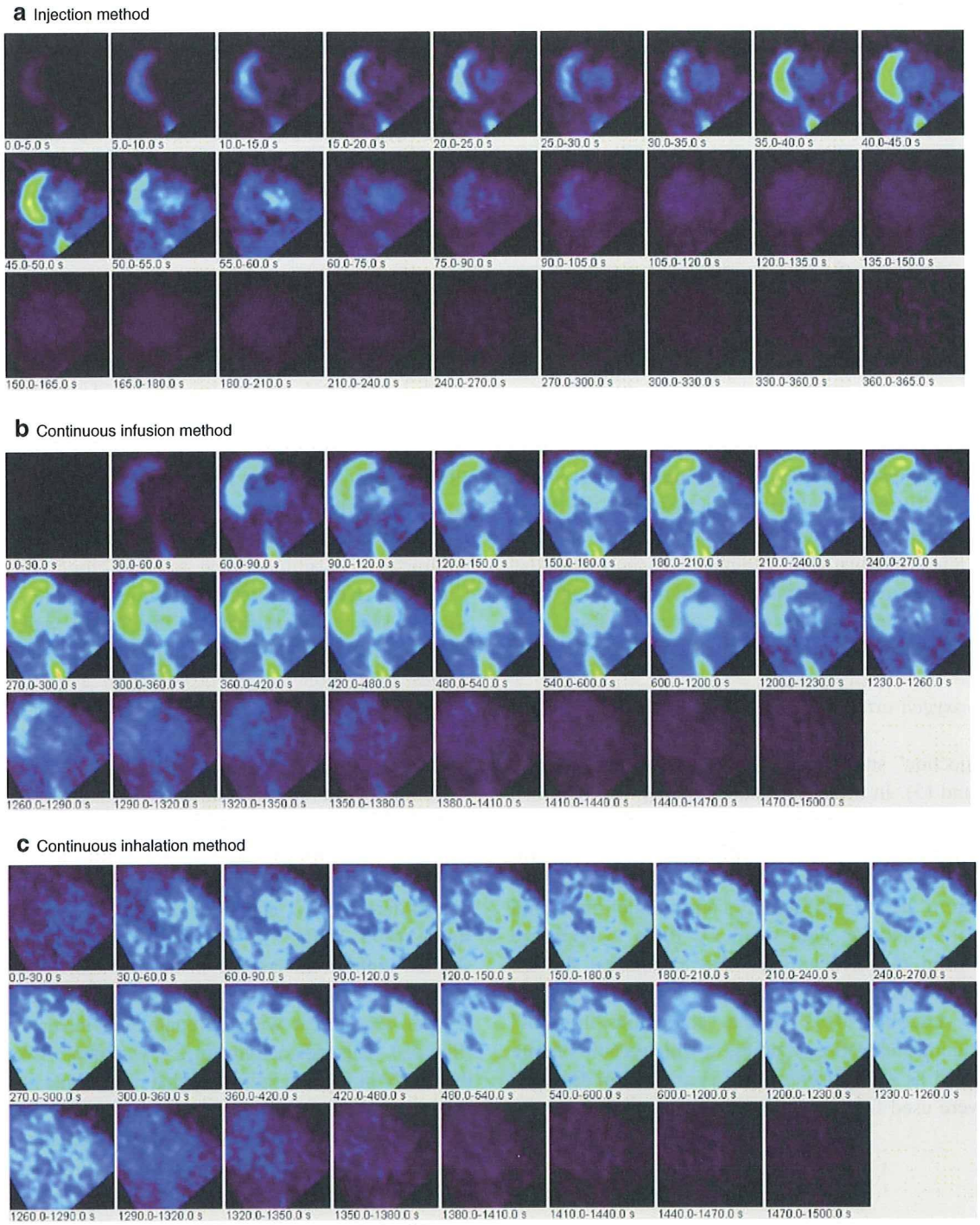

Fig. 2 PET images obtained in (**a**) the injection method, (**b**) the continuous-infusion method with injectable ^{15}O-O_2, and (**c**) the continuous-inhalation method with ^{15}O-O_2 gas

(Fig. 4b). The heart-to-lung radioactivity ratios were calculated from Fig. 4 for the quantitative estimation of image quality; the continuous-infusion method provided a ratio of 1.38±0.24, whereas the ratio was less than one with the continuous-inhalation method.

Table 2 shows the quantitative OEF values in the lateral wall obtained by the injection, continuous-infusion, and continuous-inhalation methods. These OEF values were consistent among the three methods.

Figure 5 represents the noise equivalent counts (NEC) standardized by the total counts detected by the PET scanner. Although the injection method tended to show rather high values, there was no significant difference between the values obtained by the injection and

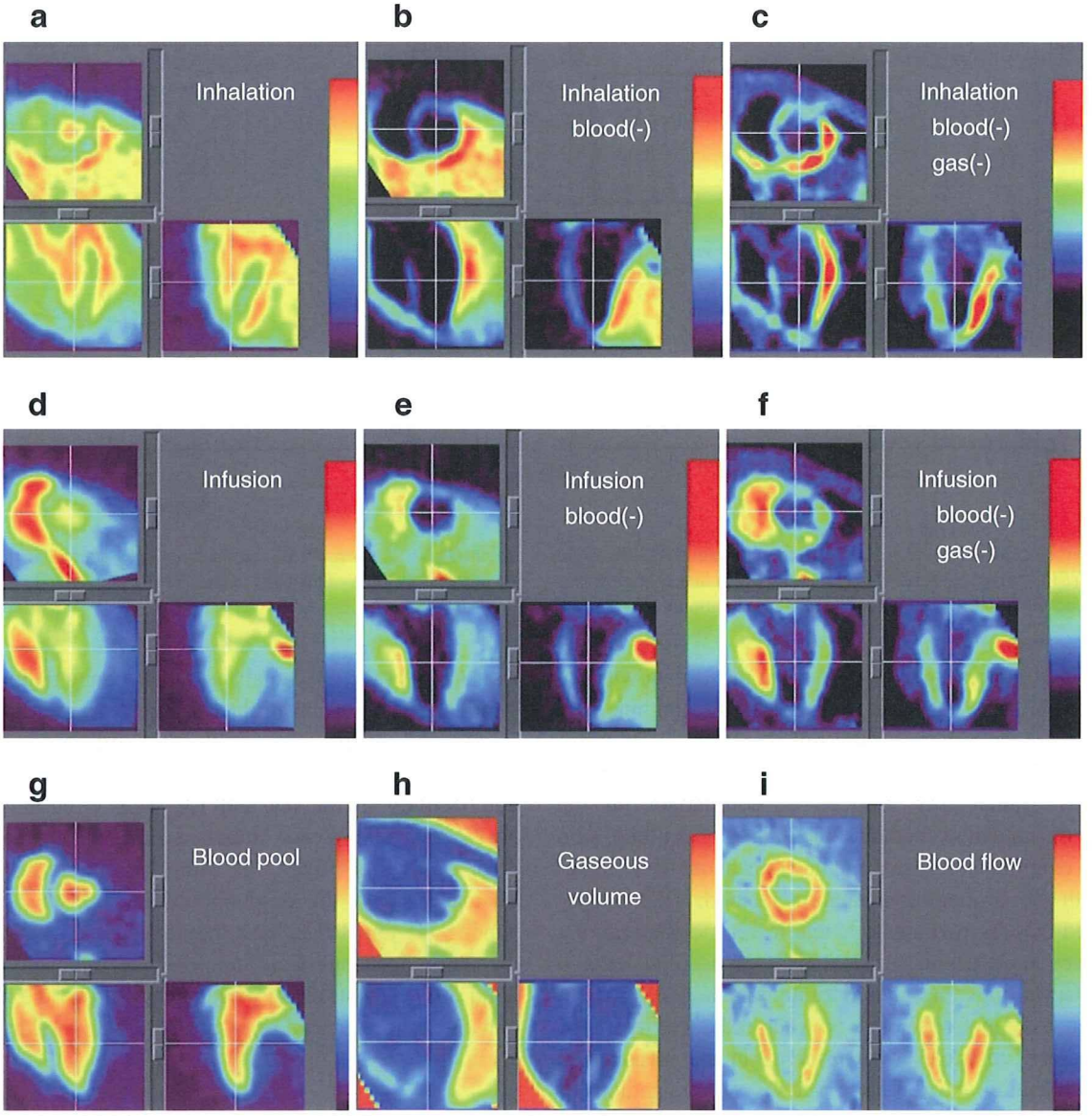

Fig. 3 PET images obtained in the study are shown. The 16th frame (steady-state frames) of the continuous-inhalation method and the continuous-infusion method are shown in (**a**) and (**d**), respectively. The 'blood-subtracted' images shown in (**b**) and (**e**) were created by subtraction of the blood-pool image by ^{15}O-CO (**g**) from (**a**) and (**d**). The 'blood- and gas-subtracted' images shown in (**c**) and (**f**) were created by the successive subtraction of the gaseous image (**h**) from (**b**) and (**e**). The myocardial blood flow image is also shown in (**i**)

continuous-infusion methods as determined by a Mann Whitney *U*-test.

Discussion

In previous studies, we showed the usefulness of the injectable ^{15}O-O_2 system for estimating cerebral oxygen metabolism in small animals such as rats under normal or ischemic conditions [10–12]. Injectable ^{15}O-O_2 replaced the inhalation protocol and radioactive ^{15}O-O_2 was administered via the tail vein. Thus, injectable ^{15}O-O_2 could abolish the artifact from the high radioactivity in the inhalation tube that distorts the PET images, especially in small animals. We considered that the concept could also be utilized in the hearts of large animals. Therefore, in the present study, we tested the feasibility of an injectable ^{15}O-O_2 system for estimating myocardial oxygen metabolism in normal pigs. In addition, since a shunt between the femoral artery and vein can be created in pigs but not in small animals, continuous infusion via the femoral shunt was also performed to achieve a constant and reliable delivery of radioactivity to the heart.

Dynamic PET scans showed a large difference in the radioactivity distribution among the three methods. Since the labeling efficiency to prepare injectable ^{15}O-O_2 was

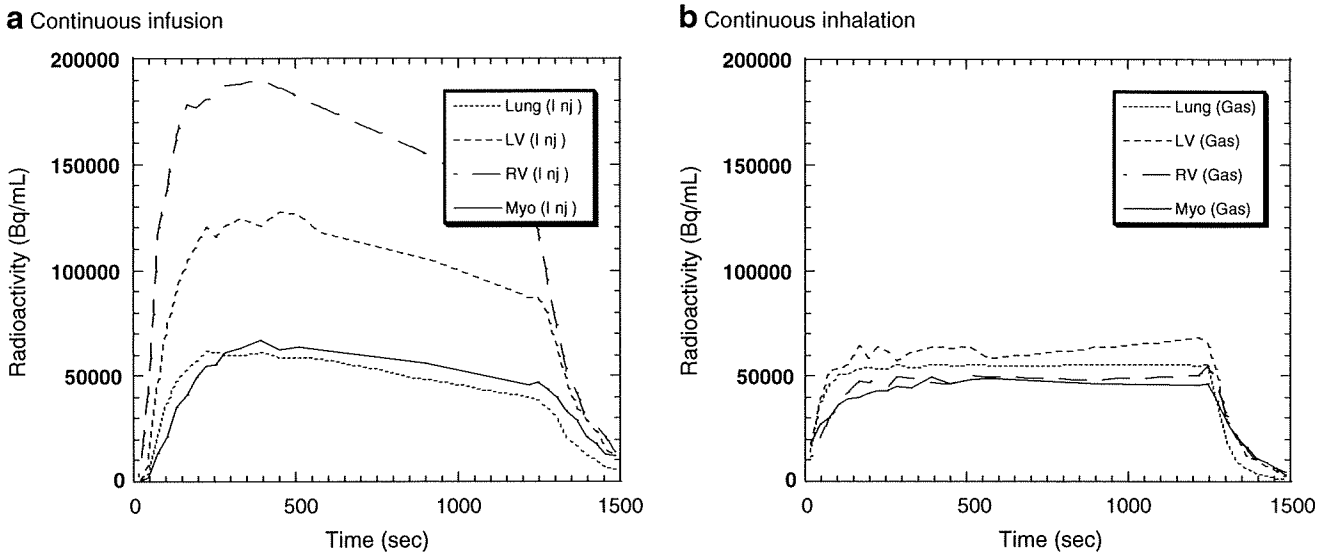

Fig. 4 Time-activity curves from the left ventricle (*LV*), the right ventricle (*RV*), the myocardium (lateral wall, Myo) and a lung region with the continuous-infusion method (**a**) and the continuous-inhalation method (**b**). The supply of radioactivity was started at time 0 s and stopped at 1,200 s. The 16th frame for the steady-state analysis was 600–1,200 s

lower with pig blood (ca. 61 MBq/ml at most) than with the blood of rats and humans (130 MBq/ml), the injection method provided rather obscure images. With the injection and continuous-infusion methods, the radioactivity in the lung was dramatically reduced in comparison to the continuous-inhalation method, since the heart-to-lung ratio with the continuous-infusion method was about 40% higher than with the continuous-inhalation method. This finding suggested that the two methods that inject radioactivity via a vein are more useful for analyzing myocardial oxygen metabolism in pigs than the continuous-inhalation method. However, a distinct difference between radioactivity of the right and left ventricles was observed in the images and time-radioactivity curves after venous administration of $^{15}O\text{-}O_2$, indicating a certain degree of excretion of the radioactivity by the lung. Therefore, the spillover from the pulmonary alveoli to the myocardium could not be omitted in the two methods with venous administration, and Eq. (4) was used for the OEF analysis, although the radioactivity in the lung was lower than that in the myocardium.

On the other hand, with the continuous-inhalation method, the radioactivity of the lung was in between the radioactivity in the RV and LV. This is curious because O-15 radioactivity was supplied from the inhalation tube and transferred from the lung to blood so that the radioactivity in the lung should have been the highest among the four ROIs. This may have been caused, in part, by inhomogeneous distribution of the radioactivity in the lung due to its structure in comparison with the myocardium and ventricles, and/or by artifacts from the lung to other

Table 2 OEF estimated by the three methods using injectable $^{15}O\text{-}O_2$ or $^{15}O\text{-}O_2$ gas

	OEF		
	Injection	Infusion	Inhalation
Pig. 1	0.70	0.72	
Pig. 2	0.67	0.72	
Pig. 3	0.71	0.74	
Pig. 4	0.76	0.69	0.72
Average	0.71	0.72	0.72
SD	0.036	0.020	

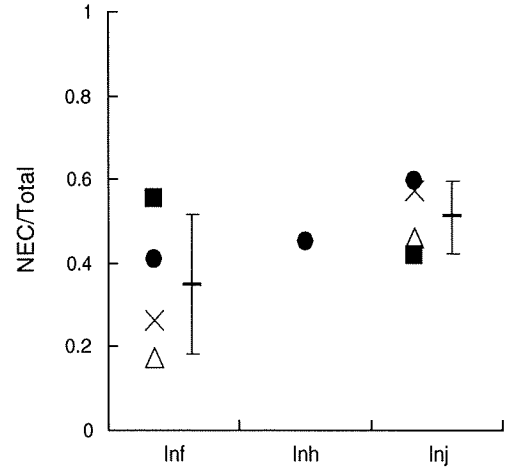

Fig. 5 The ratio of noise equivalent counts (*NEC*) to total counts in the total field of view of the PET scanner obtained with the continuous-infusion method (*Inf*), the continuous-inhalation method (*Inh*) and the injection method (*Inj*)

tissues. In any case, it is notable that the radioactivity in the myocardium was the lowest with the continuous-inhalation method, leading to difficulty in analyzing myocardial oxygen metabolism.

The OEF values in lateral walls were calculated to compare the ability of the three methods to determine myocardial oxygen metabolism by using the blood flow derived from the dual-administration protocol with the injection method and the single-administration protocol with the two continuous methods. There was no difference in the blood flow between the two protocols. Consequently, the three methods provided the same OEF value of about 0.7 and this is a physiological value in normal pigs, as was previously demonstrated [17, 18]. We have demonstrated the potential of the injectable ^{15}O-O_2 system for the estimation of physiological cerebral oxygen metabolism in rats and monkeys during early and late ischemia, hypertension, and ischemia plus hypertension [10–12, 19]. Therefore, we believe that the injection and continuous-infusion methods provide a physiological OEF in the myocardium. Nevertheless, we recognize the necessity to evaluate the reliability and usefulness of the injectable ^{15}O-O_2 method in myocardial applications. Further studies using pathophysiological animal models are required in the future, such as myocardial ischemia, hypoxia, and heart failure. On the other hand, since $MMRO_2$ is basically regarded as the product of MBF and OEF, the results indicated that these three methods were equivalent in their ability to quantify $MMRO_2$ in normal pigs, at least in the lateral wall. Although the images after the subtraction of spillovers from blood and gas showed different contrast between the continuous-infusion and continuous-inhalation methods, the ability of these two methods to measure OEF and $MMRO_2$ in the lateral walls was equivalent.

We did not evaluate myocardial oxygen metabolism in other heart regions since the radioactivity in the right ventricle could not be removed due to a significant difference of radioactivity between the ventricles with the continuous-infusion method. The injection method might be able to evaluate oxygen metabolism in other regions besides the lateral wall, although this was not evaluated in this study due to the low radioactivity of injectable ^{15}O-O_2 as described above. In the injection method, O-15 radioactivity was delivered from the femoral vein to RV, the lung, LV, and finally the myocardium. Thus, when the LV and myocardial activity reach a maximum, the RV activity is expected to be low. The later frames of the dynamic PET images with the injection method might avoid the high RV activity and delineate the myocardium and LV more clearly. With accurate anatomical information by gated PET/CT, the injection method will provide oxygen metabolism in other heart regions. In addition, the injection method has a benefit in that it is noninvasive and shortens the acquisition time in comparison with the continuous-infusion method. Future studies are needed to determine whether the injectable ^{15}O-O_2 system can be used in other heart regions.

With the injection method, the ratio of noise equivalent counts (NEC) to total counts tended to be the higher, probably because of the absence of high radioactivity adjacent to the PET scanner. Nevertheless, the continuous-infusion method did not show this tendency. This may be because tubes for the input to the artificial lung were positioned at the femoral shunt and the output to the drain of O-15 gas was positioned alongside the PET scanner, resulting in an increase of random counts during the study. Also, it is notable that the value with the continuous-inhalation method was not small, which suggests that the inhalation protocol itself did not worsen the results, but rather the high radioactivity in the lung might affect the analysis. In any case, if more care is given to shielding of the radioactivity in tubes and/or for arrangement of instruments in the PET room, a higher value of NEC/total counts will be obtained with the injectable ^{15}O-O_2 system.

The declining slope delineated in the time-activity curves with the continuous-infusion method requires some explanation. Since the flow rate of O-15 gas supply to the artificial lung positioned at the femoral shunt was maintained constant during the PET scan, it is possible that a decrease of labeling efficiency of the artificial lung occurred due to the deposition of any components of blood. The blood of rats or humans was negligibly deposited in the artificial lung during circulation at the same rate for at least 30 min in our other experiments, so that this problem may be specific for pigs. It is unclear which component in pig blood was exactly involved in the deposition and three of four pigs did not show a declining slope of the time-activity curve.

In practice, in routine studies on myocardial oxygen metabolism using large animals such as pigs, the continuous-inhalation method with ^{15}O-O_2 gas may be easier to perform for the following reasons: (1) the intubation tube used for gas anesthesia prior to the PET scan can also be used for ^{15}O-O_2 gas inhalation; (2) catheterization of the femoral artery and vein to create the femoral shunt for the continuous-infusion method may be troublesome; and (3) the injection of ^{15}O-O_2 requires an artificial lung, preparation time, and blood taken from the same animal prior to the PET scan. However, the injection of ^{15}O-O_2 has a substantial advantage over the continuous-inhalation method in that there is reduced radioactivity in the lung and clearer images of the heart are obtained. Therefore, the method for estimating myocardial oxygen metabolism should be selected depending on the objectives of the study and the surgical procedures. Furthermore, since radioactivity administered into the femoral vein is partially excreted into expired air, the injectable ^{15}O-O_2 system might be used for evaluating pulmonary function in the future.

Conclusion

In this study, we tested the feasibility of using an injectable ^{15}O-O_2 system to estimate myocardial oxygen metabolism in pigs. Both the bolus-injection and continuous-infusion methods reduced the radioactivity in the lung and provided similar OEF values in the lateral walls of the heart. These findings indicate that the injectable ^{15}O-O_2 system has the potential to evaluate myocardial oxygen metabolism.

References

1. Ohtake T. The review of myocardial positron emission computed tomography and positron imaging by gamma camera. Kaku Igaku. 1998;35:179–87.
2. Klein LJ, Visser FC, Knaapen P, Peters JH, Teule GJ, Visser CA, et al. Carbon-11 acetate as a tracer of myocardial oxygen consumption. Eur J Nucl Med. 2001;28:651–68.
3. Schelbert HR. PET contributions to understanding normal and abnormal cardiac perfusion and metabolism. Ann Biomed Eng. 2000;28:922–9.
4. Visser FC. Imaging of cardiac metabolism using radiolabelled glucose, fatty acids and acetate. Coron Artery Dis. 2001;12(Suppl 1):S12–8.
5. Hata T, Nohara R, Fujita M, Hosokawa R, Lee L, Kudo T, et al. Noninvasive assessment of myocardial viability by positron emission tomography with ^{11}C acetate in patients with old myocardial infarction. Usefulness of low-dose dobutamine infusion. Circulation. 1996;94:1834–41.
6. Yamamoto Y, de Silva R, Rhodes CG, Iida H, Lammertsma AA, Jones T, et al. Noninvasive quantification of regional myocardial metabolic rate of oxygen by $^{15}O_2$ inhalation and positron emission tomography. Experimental validation. Circulation. 1996;94:808–16.
7. Iida H, Rhodes CG, Araujo LI, Yamamoto Y, de Silva R, Maseri A, et al. Noninvasive quantification of regional myocardial metabolic rate for oxygen by use of $^{15}O_2$ inhalation and positron emission tomography. Theory, error analysis, and application in humans. Circulation. 1996;94:792–807.
8. Shidahara M, Watabe H, Kim KM, Oka H, Sago M, Hayashi T, et al. Evaluation of a commercial PET tomograph-based system for the quantitative assessment of rCBF, rOEF and rCMRO$_2$ by using sequential administration of ^{15}O-labeled compounds. Ann Nucl Med. 2002;16:317–27.
9. Mintun MA, Raichle ME, Martin WR, Herscovitch P. Brain oxygen utilization measured with O-15 radiotracers and positron emission tomography. J Nucl Med. 1984;25:177–87.
10. Magata Y, Temma T, Iida H, Ogawa M, Mukai T, Iida Y, et al. Development of injectable O-15 oxygen and estimation of rat OEF. J Cereb Blood Flow Metab. 2003;23:671–6.
11. Temma T, Magata Y, Kuge Y, Shimonaka S, Sano K, Katada Y, et al. Estimation of oxygen metabolism in a rat model of permanent ischemia using positron emission tomography with injectable ^{15}O-O_2. J Cereb Blood Flow Metab. 2006;26:1577–83.
12. Temma T, Kuge Y, Sano K, Kamihashi J, Obokata N, Kawashima H, et al. PET O-15 cerebral blood flow and metabolism after acute stroke in spontaneously hypertensive rats. Brain Res. 2008;1212:18–24.
13. Watabe H, Jino H, Kawachi N, Teramoto N, Hayashi T, Ohta Y, et al. Parametric imaging of myocardial blood flow with ^{15}O-water and PET using the basis function method. J Nucl Med. 2005;46:1219–24.
14. Iida H, Rhodes CG, de Silva R, Yamamoto Y, Araujo LI, Maseri A, et al. Myocardial tissue fraction–correction for partial volume effects and measure of tissue viability. J Nucl Med. 1991;32:2169–75.
15. Wienhard K, Dahlbom M, Eriksson L, Michel C, Bruckbauer T, Pietrzyk U, et al. The ECAT EXACT HR: performance of a new high resolution positron scanner. J Comput Assist Tomogr. 1994;18:110–8.
16. Kudomi N, Hayashi T, Teramoto N, Watabe H, Kawachi N, Ohta Y, et al. Rapid quantitative measurement of CMRO$_2$ and CBF by dual administration of ^{15}O-labeled oxygen and water during a single PET scan-a validation study and error analysis in anesthetized monkeys. J Cereb Blood Flow Metab. 2005;25:1209–24.
17. Alders DJ, Groeneveld AB, de Kanter FJ, van Beek JH. Myocardial O_2 consumption in porcine left ventricle is heterogeneously distributed in parallel to heterogeneous O_2 delivery. Am J Physiol Heart Circ Physiol. 2004;287:H1353–61.
18. Van Woerkens EC, Trouwborst A, Duncker DJ, Koning MM, Boomsma F, Verdouw PD. Catecholamines and regional hemodynamics during isovolemic hemodilution in anesthetized pigs. J Appl Physiol. 1992;72:760–9.
19. Temma T, Magata Y, Iida H, Hayashi T, Ogawa M, Mukai T, et al. Development of injectable O-15 oxygen and its application for estimation of OEF. International Congress Series, Quantitation in Biomedical Imaging with PET and MRI Proceedings of the International Workshop on Quantitation in Biomedical Imaging with PET and MRI. 2004;1265:262–65.